# Modeling and optimization of adsorption-based separation systems for improved process performance

by

Rafael Teruo Maruyama

A thesis submitted in partial fulfillment of the requirements for the degree of

Master of Science

in

CHEMICAL ENGINEERING

Department of Chemical and Materials Engineering

University of Alberta

# Abstract

This thesis focuses on two different separation processes based on adsorption. The first part focuses on column chromatography and simulated moving bed (SMB) operations for liquid-phase separations. The second part focuses on the separation of gas mixtures for $CO_2$ capture applications.

The first part of this thesis analyzes simulated moving bed chromatography operated with bypass lines for processes with reduced purity constraints. Initially, the system is thoroughly analyzed based on the local-equilibrium theory, considering ideal conditions and linear isotherms. It is then followed by computational analysis of different case studies considering a non-ideal column and non-linear isotherms. Specific conditions, under which the process performance improves, are illustrated.

The second part focuses on the modeling, validation and optimization of $CO_2$ capture through pressure swing adsorption (PSA) and it was divided into two chapters. It initially studies of the effects of reduced $CO_2$ constraints in post-combustion $CO_2$ capture with PSA. In this scenario, the greenhouse gas is captured from a mixture of $N_2$ and $CO_2$ and the impact of the reduced recovery constraint is studied by analyzing the resulting energy consumption and process productivity. It is then followed by a study that focus on the modeling of a $CO_2$ capture unit installed in an Integrated Gasification Combined Cycle (IGCC) power plant, based on a capture unit operated by TDA Research Inc. The unit is composed of eight adsorption columns working in parallel, where the desired gas is captured from a mixture of $H_2$ and $CO_2$. The simulation results are compared with the data measured on the field for validation.

**Keywords:** process modeling and optimization, simulated moving bed, bypass, carbon dioxide capture, vacuum swing adsorption, reduced recovery.

# Preface

This thesis is an original work of Rafael Teruo Maruyama under the supervision of Dr. Arvind Rajendran and is written in a paper format.

Chapter 2 of this thesis has been published as R. T. Maruyama, P. Karnal, T. Sainio and A. Rajendran, "Design of bypass-simulated moving bed chromatography for reduced purity requirements", *Chem. Eng. Sci.*, vol. 205, 401-413, 2019. I was responsible for validating the theoretical calculations with a detailed computational model, system optimization, grid search, data collection, analysis of the results and manuscript composition. T. Sainio was involved with the concept formation and problem analysis. P. Karnal and A. Rajendran were responsible for the explicit equations and the results based on the equilibrium-theory analysis solution. A. Rajendran was also the supervisory author, involved with the concept formation and manuscript composition.

Chapter 3 of this thesis will be submitted for publication as R. T. Maruyama, K. N. Pai, S. G. Subraveti, and A. Rajendran, "Improving the performance of VSA based $CO_2$ capture for reduced recovery requirements: doing more by doing less". I was responsible for the modeling, multi-objective optimization, data collection, analysis of the results and manuscript composition. K. N. Pai and S. G. Subraveti were involved with the concept formation and manuscript composition. A. Rajendran was the supervisory author and was involved with the concept formation and manuscript composition.

*To my parents*

# Acknowledgements

I would like to thank Dr. Arvind Rajendran for the opportunity, support and trust throughout my Master's of Science degree and my exchange program at the University of Alberta during my undergraduate degree. With his support and guidance, I was able to accomplish my initial goals and extend them to much higher levels. Every individual and group meeting provided the support necessary to build a vast repertoire of skills for a well-rounded and successful engineer.

I also would like to thank my colleagues Kasturi Nagesh Pai, Libardo Perez, Nicholas Wilkins, Sai Gokul Subraveti, Nguyen Tai and Vishal Subramanian Balashankar for their friendship throughout my graduate program and for the countless times that I could learn with their different cultural backgrounds, experiences and vast scientific knowledge.

I acknowledge the funding received from the United States Department of Energy, TDA Research Inc. and the University of Alberta Future Energy Systems to support my research. I would like to thank TDA Research Inc. once again for their support and industrial partnership throughout the pre-combustion $CO_2$ capture project.

Finally, I would like to thank my parents, Marlete and Eduardo, for their love, trust, unconditional support and for teaching me that with hard work and a good heart nothing is impossible.

Rafael Teruo Maruyama
Edmonton 2019

# Contents

# List of Tables

# List of Figures

# List of Symbols

## Roman symbols

| | |
|---|---|
| $b$ | adsorption equilibrium constant for high energy site [ $m^3$ $mol^{-1}$ ] |
| $c$ | fluid phase concentration of solute [ g $L^{-1}$ ] |
| $d$ | adsorption equilibrium constant for low energy site [ $m^3$ $mol^{-1}$ ] |
| $D_L$ | axial dispersion coefficient [ $cm^2$ $s^{-1}$ ] |
| $E$ | energy [ kWh ] |
| $H$ | Henry constant |
| $k$ | adsorption equilibrium constant [ $m^3$ $mol^{-1}$ ] |
| $K$ | equilibrium constant in Langmuir isotherm [ L $g^{-1}$ ] |
| $L$ | length of column [cm] |
| $m$ | dimensionless flow rate ratio |
| $n$ | number of moles |
| $N$ | number of columns |
| $N_{tot}$ | total number of columns |
| $Pu$ | product purity [ % ] |
| $Pr$ | productivity [ g $g^{-1}$ $s^{-1}$ ] |
| $\Delta P_{\max}$ | maximum allowed pressure drop [ bar ] |
| $Q$ | volumetric flow rate [ $cm^3$ $s^{-1}$ ] |
| $q^*$ | solid phase equilibrium concentration of solute [ g $L^{-1}$ ] |
| $q_s$ | saturation solid phase concentration [ mol $kg^{-1}$ ] |
| $Re$ | product recovery [ % ] |
| $s$ | homogeneity of the adsorbent's surface |
| $t$ | time [ s ] |
| $t^*$ | switch time [ s ] |
| $T$ | temperature [ K ] |
| $\Delta U$ | internal energy [ J $mol^{-1}$ ] |
| $v$ | interstitial velocity [ cm $s^{-1}$ ] |

| | |
|---|---|
| $V$ | volume of column [ $cm^3$ ] |
| $V^{BP}$ | bypassed volume [ $cm^3$ ] |
| $x$ | molar fraction [-] |
| $y$ | molar fraction [ - ] |
| $z$ | axial coordinate [ cm ] |

## Abbreviations, subscripts and superscripts

| | |
|---|---|
| ADS | adsorption |
| BD | blowdown |
| D | desorbent |
| E | extract |
| EQD | pressure equalization donor |
| EQR | pressure equalization receiver |
| EVAC | evacuation |
| F | feed |
| $i$ | component |
| $j$ | SMB section |
| LPP | light product pressurization |
| PRESS | pressurization |
| PU | purge |
| R | raffinate |
| ref | reference |
| tgt | product target |

## Greek symbols

| | |
|---|---|
| $\alpha$ | selectivity |
| $\gamma$ | adiabatic constant |
| $\varepsilon$ | column void fraction |
| $\eta$ | pump efficiency |
| $\Theta$ | desorbent requirement ratio between BP-SMB and RP-SMB |
| $\Lambda$ | productivity ratio between BP-SMB and RP-SMB |
| $\Lambda_{max}$ | maximum productivity ratio |
| $\nu$ | phase ratio, (1-$\varepsilon$)/$\varepsilon$ |
| $\phi$ | permeability [ bar s $cm^{-2}$ ] |

# Chapter 1

# Introduction

## 1.1 Adsorption-based separation processes

Adsorption is a phenomenon characterized by the affinity between sites present in porous solids and certain molecules, which result in the latter being adhered on the surface of the adsorbent. Based on the nature of the bond between the adsorbent and the adsorbate, adsorption can be divided into two main groups: physisorption for scenarios where the bond is formed by relatively weak forces, usually originated from polarization between molecules (e.g. van der Waals and electrostatic forces) and chemisorption for situations where the adsorbed molecule chemically interacts with the adsorbent, forming stronger covalent bonds. Considering these characteristics, adsorption has been thoroughly studied for decades as a potential option to separate different mixtures in small and large scale operations [2].

### 1.1.1 Elution and simulated moving bed chromatography

Elution chromatography is a practical application of an adsorption-based separation process, where the interaction between the adsorbent (i.e. stationary phase packed in a column) and the mixture (i.e. mobile phase) results in the components present in the fluid phase to travel at different velocities, enabling their separation. In summary, the feed is injected at the inlet of the column in intermittent steps and as it travels through the bed, the different levels of interaction between the adsorbent and the molecules in the fluid phase create regions with different concentrations. By timing the capture of the outlet stream, the different compounds in the mixture can be collected separately. It is a process commonly used in pharmaceutical and cosmetics industries, where highly pure products are required (e.g. enantiomer separations in the pharmaceutical industry) [3].

One drawback of elution chromatography is its intermittent nature. One technology used to

overcome this problem is the utilization of simulated moving beds (SMB). SMB is characterized by having multiple chromatographic columns used in series with its inlets and outlets switching positions at specific times. The final result has the objective of simulating the movement of the stationary phase through the column, increasing the bed utilization and turning the previous intermittent process into a continuous one.

### 1.1.2 $CO_2$ capture

In recent years, the utilization of adsorbents to separate and purify gases has been growing, including its usage on carbon capture and storage (CCS) [4]. This is done by a single or a group of adsorption columns, where one or more different types of adsorbents are placed in it and used to capture the target molecule, which in CCS is mainly $CO_2$. In order to regenerate the column and extract the captured molecules, a desorption stage is then used. Considering the characteristics of the process and how the adsorption and desorption steps are executed, the process can be classified into pressure swing adsorption (PSA) or temperature swing adsorption (TSA). This thesis will focus only on PSA systems, where the $CO_2$ molecules are adsorbed at high pressures (where the adsorbent presents higher solid loading concentration) and then desorbed at low pressures (hence, lower solid loading concentration). Working capacity is the difference between solid loading concentrations and is highly impactful in the material and cycle performances.

$CO_2$ capture technologies can be divided into three main categories: post-combustion, pre-combustion and oxy-fuel combustion. The latter is characterized by the combustion of a fuel with pure $O_2$ from an air separation unit. At the end, only $CO_2$ is generated, hence, it can be directly pressurized and sent to storage. This technology will not be further portrayed in this work.

Post-combustion $CO_2$ capture is characterized by capturing $CO_2$ from the flue gas originated from the combustion of fossil fuels in power plants. The exhaust gas tends to be at around 40°C and atmospheric pressure. The concentration of $CO_2$ in this condition is between 8% and 15%, varying depending on the type of fossil fuel burned. This technology presents a relatively high level of maturity, with large-scale separation units in operation around the world [5]. Considering that this process does not require thermal energy, retrofitting power plants already in operation tends to be a viable option as well [6].

On the other hand, pre-combustion $CO_2$ capture is a process where the target molecule is captured from synthesis gas (i.e. a gas mixture mainly composed of $H_2$ and $CO_2$) originated from the gasification of coal or other fossil fuel material, resulting in a high $CO_2$ concentrated solution. Synthesis gas tends to have around 35% $CO_2$ in its composition. Considering that at

the end of gasification, the synthesis gas is usually at relatively high pressures and temperatures (e.g. 200°C and 20 bar), plenty of different cycle configurations and operating conditions can be explored, which increases the process flexibility. In comparison with post-combustion, pre-combustion capture presents a bigger margin of improvement considering its current level of maturity [6]. Moreover, this process presents a high potential for improvements, where computational optimization can be used to reduce energy consumption levels and the overall costs.

## 1.2 Solid adsorbents

The selection of the solid adsorbent used in the separation process is a crucial step when designing the equipment. Different characteristics of the material and its interaction with the equipment and the compounds present in the separation mixture should be considered (e.g. solid loading concentration, working capacity, selectivity, mechanical and chemical stability and price). In this work, three different types of adsorbent will be used and an overview of each individual material is presented below.

### 1.2.1 Zeolites

Zeolites are a group of porous crystalline alumninosilicate materials formed by the union of $SiO_4$ and $AlO_4$ bonded through shared oxygen connections in tetrahedral structures [2]. Zeolite structures can have both natural or artificial origins, with more than 170 materials already synthesized [7]. Between all the different types of zeolites, Zeolite 13X is a material that found great success in $CO_2$ capture, presenting high performance at relatively low prices and is commonly used as a material benchmark in adsorption separations [8]. It is worth mentioning though that zeolites tend to have high selectivity towards $H_2O$, requiring dry gas mixtures in order to operate effectively.

### 1.2.2 Activated carbons

Activated carbon is a type of adsorbent produced from carbonaceous materials (e.g. coal, biomass) after high temperature activation through steam or carbon dioxide. The activation has the objective of removing tarry products and to open the pores in the solid material [2]. This adsorbent can be used in plenty of different separation processes, including water purification, organic compounds recovery and gas separation. The surface area and pores sizes tend to vary depending on the synthesis procedure and choice of carbonaceous material. Activated carbon presents relatively low production costs and are reasonably hydrophobic, hence, enabling its utilization in $CO_2$ capture in humid conditions.

### 1.2.3 Metal-organic frameworks

Metal-organic frameworks (MOF) are porous synthetic crystalline materials characterized by the presence of inorganic metal ions connected with organic ligands. This type of material is relatively new and very promising in plenty of different engineering areas, including CCS. This adsorbent is very flexible and presents the potential to be tailor-made depending on the required characteristics due to the multiple possible combinations between the metal ions and organic ligands in its composition. Although plenty of MOFs present high carbon dioxide selectivity and working capacity, their mechanical and chemical stability, the effect of impurities in the feed and the practical aspects in adsorption columns are still a challenge [6]. UTSA-16 is a type of MOF that presented promising characteristics for gas separation in recent studies, with great potential for $CO_2$ capture in PSA systems [9].

## 1.3 Thesis objectives and outline

The goal of this thesis is to study the aspects of solid adsorption-based separation systems with different product purity and recovery constraints. The thesis focuses on the computational modeling, validation, analysis and optimization of different adsorption-based separation processes and it can be divided into two main parts. The first part (i.e. chapter 2) focuses on the operation of simulated moving beds (SMB) with bypass lines for systems with reduced purity constraints. The second part (i.e. chapters 3 and 4) presents a detailed study of adsorption-based $CO_2$ capture through pressure swing adsorption (PSA) in both pre-combustion and post-combustion scenarios.

Chapter 2 studies the characteristics of operating SMBs with bypass lines in systems with reduced purity requirements. Based on the local-equilibrium theory, explicit equations to calculate productivity are derived for systems following a linear isotherm. The effects of column efficiency and feed concentration for systems following non-linear isotherms are studied using numerical simulations. Productivity and energy consumption are calculated and used as performance indicators and a thorough grid search optimization is used to find the operating conditions with the best performances. Bypass-SMB (BP-SMB) is then compared with regular SMB operations.

Chapter 3 analyzes the effect of reduced recovery constraints in PSA systems for post-combustion $CO_2$ capture from the exhaust gas of power plants. The $CO_2$ product purity, energy consumption and productivity are calculated from computational simulations and used as performance indicators. The best operating conditions are obtained through multi-objective optimization and Pareto fronts are used to analyze the trade-off between energy consumption and productivity. It initially focuses on $CO_2$ capture with a 4-step VSA cycle with light product pressurization and zeolite 13X. Other case studies, including different solid adsorbents, feed compositions and

vacuum pump efficiencies are included for a thorough analysis of the phenomenon's extent.

Chapter 4 introduces a methodology used to computationally model a pilot-scale unit composed of a system of eight adsorption columns working in parallel that capture $CO_2$ from an IGCC power plant. The results obtained from the simulations are studied and validated with the data measured on site from a $CO_2$ capture unit that was operated by TDA Research Inc. in Alabama, USA.

Finally, chapter 5 presents the final conclusions of this work and also an overview of possible future studies.

# Chapter 2

# Design of bypass-simulated moving bed chromatography for reduced purity requirements [1]

## 2.1 Introduction

Chromatographic processes are often used for separations that result in products of very high purities e.g., enantiomer separations [10]. The simulated moving bed chromatography (SMB) process that was originally developed for petrochemical separations was later expanded to sugar separations and to pharmaceutical purifications [11, 12]. The ability of the SMB to produce high-purity products, at high-productivity and reduced solvent consumption, with the use of low-efficiency columns was one of the primary reasons for its rapid acceptance in the industry. In the last 20 years, the technology has matured with proven applications in binary and ternary separations [3, 13].

The study of SMB has focused on designing the process for high-purities (excess of 99%). However, there are situations where the SMB is tasked with the production of reduced purity products, i.e., purity $< 100\%$. This happens in the case of hybrid processes where the SMB performs the bulk separation and another process, e.g., crystallization, purifies the product further [10,14] and in processes where lower purity products have commercial value, e.g., the production of high-fructose corn syrup (HFCS) [10]. In HFCS separation, the outlet of an isomerization reactor containing 42% fructose and 58% glucose, is fed to a SMB. The feed is resolved into a raffinate

[1] This chapter has been published as R. T. Maruyama, P. Karnal, T. Sainio and A. Rajendran, "Design of bypass-simulated moving bed chromatography for reduced purity requirements", *Chem. Eng. Sci.*, vol. 205, 401-413, 2019.

stream that has a glucose purity of 90% and an extract with fructose purity of 55%. The extract is the product of commercial interest, while the raffinate product is recycled to the isomerization reactor. In practice, this separation is operated in an interesting manner, where the extract product is over-purified, e.g., up to a purity of 90% fructose and is blended with the feed stream that is "bypassed" in order to produce the target 55% HFCS product [10]. This configuration, that will be referred to as "Bypass SMB" (BP-SMB), provides additional degrees of freedom to produce low purity products by over-purifying them with the feed to reach the target-purity. Siitonen et al. described a single-column version of this concept (bypass chromatography) and developed explicit design methods for systems that follow linear and Langmuir isotherms [15,16]. They also explored conditions under which bypass chromatography provides advantages over a chromatographic separation that directly provides products that meet the target purities. It was shown that the productivity of bypass chromatography was superior to the reduced purity chromatography process under the following conditions: when low purities of the two products are required; when the feed composition is further from being an equimolar mixture, when the total concentration of the feed is low and when the column efficiency is high.

The main goal of this manuscript is to extend the analysis of the bypass-chromatography to that of BP-SMB. Explicit design equations are developed within the framework of the triangle-theory, for the case of linear isotherms [12, 17]. Numerical simulations are used to validate the design method and extend it to the case of non-linear isotherms. Case studies are performed in order to identify conditions under which the BP-SMB provides advantage over the classical SMB. The case of HFCS manufacture is discussed in detail.

## 2.2 Bypass-SMB: System description and modeling

### 2.2.1 System description

The system considered in this study is described in Fig. 2.1. It consists of a classical four-section SMB with the provision of using multiple columns in each section coupled with a blending section. The feed consists of a binary mixture of two species: the strongly adsorbing component "A" and the weekly adsorbing component "B" dissolved in a non-adsorbing desorbent. The concentration of component $i$ in the feed is ${c_i}^{\mathrm{F}}$. The feed is introduced between sections 2 and 3, which perform the separation duty. Sections 1 and 4 are responsible for regenerating the solid and fluid phases, respectively. The desorbent is introduced into section 1 and leaves section 4. In many practical situations, the desorbent leaving section 4 is externally regenerated to remove the impurities and recycled to section 1. In this work, we restrict ourselves to the case of an open-loop configuration, i.e., one in which the desorbent is not recycled. The raffinate product, which consists of the product enriched in B, is recovered between sections 3 and 4, while the extract product, which

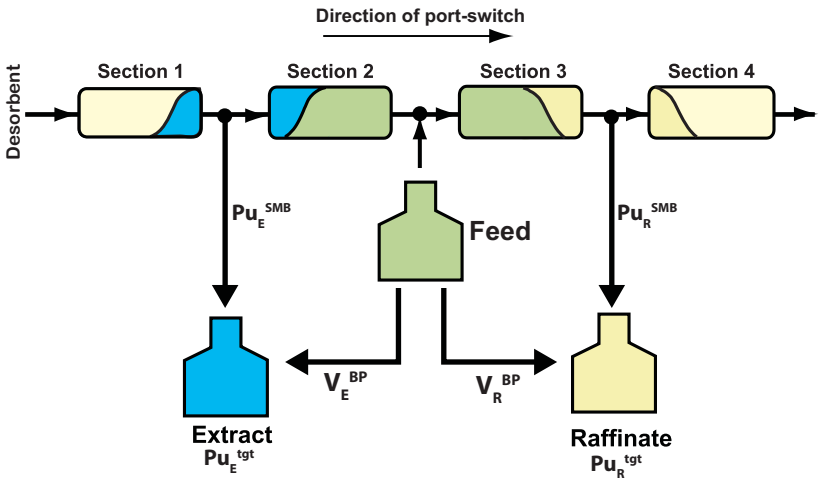


Figure 2.1: Schematic of the Bypass-SMB concept

is enriched in A, is recovered between sections 1 and 2. The inlet and outlet ports are switched in the direction of the fluid flow to simulate the countercurrent movement of the solid and fluid phases. In the current case, the purity of the extract and raffinate streams obtained from the SMB, denoted as $Pu_{\mathrm{E}}^{\mathrm{SMB}}$ and $Pu_{\mathrm{R}}^{\mathrm{SMB}}$, respectively are defined as:

$$Pu_{\mathrm{E}}^{\mathrm{SMB}} = \frac{n_{\mathrm{A,E}}^{\mathrm{SMB}}}{n_{\mathrm{A,E}}^{\mathrm{SMB}} + n_{\mathrm{B,E}}^{\mathrm{SMB}}} \tag{2.1}$$

and

$$Pu_{\mathrm{R}}^{\mathrm{SMB}} = \frac{n_{\mathrm{B,R}}^{\mathrm{SMB}}}{n_{\mathrm{A,R}}^{\mathrm{SMB}} + n_{\mathrm{B,R}}^{\mathrm{SMB}}} \tag{2.2}$$

In the above equations, $n$ represents the number of moles of a particular species collected within one switch (the switch time is denoted as $t^*$).

The SMB is considered to have identical columns, each of length $L$, volume $V$ and void fraction $\varepsilon$. Each section of the SMB has a unique internal flow rate $Q_j$, with $j = 1...4$ representing the different sections of the SMB. The internal and external flow rates are related by the following nodal balances:

$$Q_1 = Q_{\mathrm{D}} \tag{2.3}$$

$$Q_2 = Q_1 - Q_{\mathrm{E}} \tag{2.4}$$

$$Q_3 = Q_2 + Q_{\mathrm{F}} \tag{2.5}$$

$$Q_4 = Q_3 - Q_{\mathrm{R}} \tag{2.6}$$

The difference between a reduced purity SMB (RP-SMB), a process where the SMB produces the target products, and a BP-SMB is the flexibility to blend the feed with either one, or both,

products in order to reach the target purities of the process, $Pu_{\mathrm{E}}^{\mathrm{tgt}}$ and $Pu_{\mathrm{R}}^{\mathrm{tgt}}$. In the case of RP-SMB, $Pu_{\mathrm{E}}^{\mathrm{SMB}} = Pu_{\mathrm{E}}^{\mathrm{tgt}}$ and $Pu_{\mathrm{R}}^{\mathrm{SMB}} = Pu_{\mathrm{R}}^{\mathrm{tgt}}$, while in the case of BP-SMB $Pu_{\mathrm{E}}^{\mathrm{SMB}} \geq Pu_{\mathrm{E}}^{\mathrm{tgt}}$ and $Pu_{\mathrm{R}}^{\mathrm{SMB}} \geq Pu_{\mathrm{R}}^{\mathrm{tgt}}$. The volume of feed bypassed to the extract and raffinate products, denoted as $V_{\mathrm{E}}^{\mathrm{BP}}$ and $V_{\mathrm{R}}^{\mathrm{BP}}$, respectively can be be calculated as:

$$V_{\mathrm{E}}^{\mathrm{BP}} = \frac{Pu_{\mathrm{E}}^{\mathrm{tgt}} \left( n_{\mathrm{A,E}}^{\mathrm{SMB}} + n_{\mathrm{B,E}}^{\mathrm{SMB}} \right) - n_{\mathrm{A,E}}^{\mathrm{SMB}}}{{c_{\mathrm{A}}}^{\mathrm{F}} - Pu_{\mathrm{E}}^{\mathrm{tgt}} \left( {c_{\mathrm{A}}}^{\mathrm{F}} + {c_{\mathrm{B}}}^{\mathrm{F}} \right)} \tag{2.7}$$

$$V_{\mathrm{R}}^{\mathrm{BP}} = \frac{Pu_{\mathrm{R}}^{\mathrm{tgt}} \left( n_{\mathrm{A,R}}^{\mathrm{SMB}} + n_{\mathrm{B,R}}^{\mathrm{SMB}} \right) - n_{\mathrm{B,R}}^{\mathrm{SMB}}}{{c_{\mathrm{B}}}^{\mathrm{F}} - Pu_{\mathrm{R}}^{\mathrm{tgt}} \left( {c_{\mathrm{A}}}^{\mathrm{F}} + {c_{\mathrm{B}}}^{\mathrm{F}} \right)} \tag{2.8}$$

## 2.3 Modelling

From the above description, it is evident that BP-SMB is nothing but a standard SMB coupled with a blending step. In order to numerically simulate the operation of a SMB, the following assumptions are made:

1. There are no radial concentration gradients along the columns.
2. The system is isothermal.
3. Fluid velocity is constant in each column.
4. Column properties are constant and identical throughout the unit.
5. Local equilibrium is assumed between fluid and solid concentrations.
6. All mass transfer effects are modelled using the axial dispersion coefficient.

The above set of assumptions result in what is traditionally referred to as the 1D equilibrium-dispersive model. The component mass balance is provided by :

$$D_{L,i,j} \frac{\partial^2 c_i}{\partial z^2} - v_j \frac{\partial c_i}{\partial z} - \frac{\partial}{\partial t} \left[ c_i + \frac{1-\varepsilon}{\varepsilon} q_i^* \right] = 0 \tag{2.9}$$

where $v_j$ is the interstitial fluid velocity in section $j$, $\varepsilon$ is the column void fraction, $q_i^*$ is the solid phase loading in equilibrium with the fluid phase concentration $c_i$, and $D_{L,i,j}$ is the velocity-dependent axial dispersion coefficient. The above equation can be solved using a set of initial conditions and the well-known Danckwert's boundary conditions [12]. For a specific set of operating conditions, the SMB can be simulated by writing a component balance for each of the solutes and coupling the mass balances with the nodal balances. The SMB process is simulated until cyclic steady state is reached and all performance indicators are calculated under this condition. In this work, Eq. 2.9 was discretized in the axial direction using a finite volume technique, where each column was divided into 50 control volumes. The resulting ordinary differential equation was then solved using the built-in MATLAB solver *ode45*.

## 2.4 Design of reduced-purity SMBs

The design of classical SMB can be performed using the well-known "triangle-theory" [12, 17], which is based on the equilibrium theory of chromatography [18, 19]. The design is based on the concept of a true-moving bed (TMB) together with the application of the SMB-TMB equivalence relationships. The triangle theory relies on the concept of the dimensionless flow rate ratios, $m_j$, defined for each section of the SMB:

$$m_j = \frac{Q_j t^* - V\varepsilon}{V(1-\varepsilon)} \tag{2.10}$$

For systems that follow a linear isotherm, i.e., when:

$$q_i^* = H_i c_i \tag{2.11}$$

where $H_i$ is the Henry constant of component $i$, the necessary conditions to ensure complete separation, i.e. $Pu_{\mathrm{E}}^{\mathrm{SMB}} = Pu_{\mathrm{R}}^{\mathrm{SMB}} = 100\%$, while satisfying solid and fluid phase regeneration requirements, is given by the set of constraints:

$$H_A \leq m_1 \tag{2.12}$$

$$H_B < m_2 \leq H_A \tag{2.13}$$

$$H_B \leq m_3 \leq H_A \tag{2.14}$$

$$m_4 \leq H_B \tag{2.15}$$

The constraints on $m_2$ and $m_3$ can be plotted as shown in Fig. 2.2. In this figure, the triangular region RSU represents the space where constraints on $m_2$ and $m_3$ are fulfilled. Operating within this triangular region, while simultaneously satisfying constraints on $m_1$ and $m_4$, guarantees the complete separation of the feed into pure extract and raffinate streams. From the definition of $m_j$, it can be immediately recognized that the difference $m_3 - m_2$ is proportional to the feed flow and hence the vertex of the triangle, i.e., point "U", represents the operating condition that maximizes the productivity.

Rajendran derived explicit design equations for linear RP-SMB [20]. The regions on the $m_2 - m_3$ plane that guarantee a purity of $Pu_{\mathrm{E}}^{\mathrm{SMB}}$ (with $Pu_{\mathrm{E}}^{\mathrm{SMB}} < 100\%$) and $Pu_{\mathrm{R}}^{\mathrm{SMB}}$ (with $Pu_{\mathrm{R}}^{\mathrm{SMB}} < 100\%$) are given by the line segments "STP" and "RQP", respectively. It is worth noting that while there is a wide operating range to obtain complete separation, there is just one unique location where target reduced purities can be achieved for both extract and raffinate, i.e., point P. This situation makes the production of reduced purity products directly from the SMB very challenging. The space within the pentagonal region "PQRST" guarantees that the extract

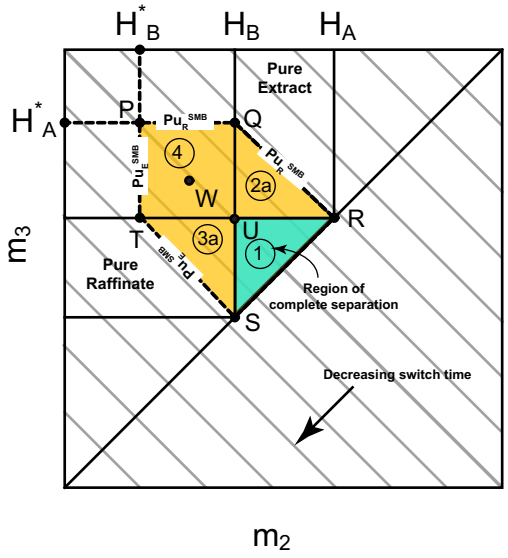


Figure 2.2: Separation regions for a SMB operated under reduced purities using the equilibrium theory of chromatography. The family of parallel lines for constant $t^*$ is obtained from Eq. 2.26

and raffinate products are at purities greater than $Pu_{\mathrm{E}}^{\mathrm{tgt}}$ and $Pu_{\mathrm{R}}^{\mathrm{tgt}}$. This region can be easily constructed by calculating two auxiliary Henry constants $H_{\mathrm{A}}^*$ and $H_{\mathrm{B}}^*$ defined as:

$$H_{\mathrm{A}}^* = \frac{H_{\mathrm{B}} {c_{\mathrm{B}}}^{\mathrm{F}} (Pu_{\mathrm{R}}^{\mathrm{tgt}} - 1) + H_{\mathrm{A}} {c_{\mathrm{A}}}^{\mathrm{F}} Pu_{\mathrm{R}}^{\mathrm{tgt}}}{{c_{\mathrm{B}}}^{\mathrm{F}} (Pu_{\mathrm{R}}^{\mathrm{tgt}} - 1) + {c_{\mathrm{A}}}^{\mathrm{F}} Pu_{\mathrm{R}}^{\mathrm{tgt}}} \tag{2.16}$$

$$H_{\mathrm{B}}^* = \frac{H_{\mathrm{B}} {c_{\mathrm{B}}}^{\mathrm{F}} Pu_{\mathrm{E}}^{\mathrm{tgt}} + H_{\mathrm{A}} {c_{\mathrm{A}}}^{\mathrm{F}} (Pu_{\mathrm{E}}^{\mathrm{tgt}} - 1)}{{c_{\mathrm{B}}}^{\mathrm{F}} Pu_{\mathrm{E}}^{\mathrm{tgt}} + {c_{\mathrm{A}}}^{\mathrm{F}} (Pu_{\mathrm{E}}^{\mathrm{tgt}} - 1)} \tag{2.17}$$

In this case, the maximum productivity is achieved by operating the SMB at point "P". While the determination of the region of complete separation for common non-linear isotherms such as the Langmuir isotherm can be obtained in an explicit form [21], the calculation of boundaries for reduced purities is so far possible only through numerical simulations [22, 23].

Once the physical dimensions of the SMB are fixed, the design of SMB requires the calculation of the four internal flow rates, $Q_j$ and the switch time, $t^*$. In order to explicitly calculate these parameters, for the case of complete separation, the four design constraints, i.e. Eqs. 2.12 to 2.15 along with a fifth constraint are used. For the case of reduced purity products Eqs. 2.12, 2.15, along with the values of $m_2$ and $m_3$ chosen within the region "PQRST" and a fifth constraint are used. The fifth constraint in both cases, is usually based either on an expression that provides flow rates that corresponds to the maximum permissible pressure drop or from the van Deemter curve that provides the condition for the flows in order to achieve the optimal column efficiency. In this work, we use the constraint based on the maximum pressure drop, which is often referred

to as a the minimum switch time design [24, 25]. Here, $t^*$ is calculated by:

$$t^* = \frac{\phi L^2}{\Delta P_{max}} \sum_{j=1}^{4} N_j (m_j(1-\varepsilon)+\varepsilon) \tag{2.18}$$

where $\phi$ is the permeability and $\Delta P_{max}$ is the maximum allowable pressure drop. Finally, once $m_j$ and $t^*$ are calculated, the external flow rates can be determined, using the nodal balances (Eqs. 2.3 to 2.6) and the SMB can be operated. Productivity, $Pr^{\mathrm{SMB}}$, can be calculated as

$$Pr^{\mathrm{SMB}} = \frac{(m_3 - m_2)}{N_{\mathrm{tot}} t^*_{SMB}} ({c_{\mathrm{A}}}^{\mathrm{F}} + {c_{\mathrm{B}}}^{\mathrm{F}}) \tag{2.19}$$

and the desorbent requirement, $DR^{\mathrm{SMB}}$, can be calculated as

$$DR^{\mathrm{SMB}} = \frac{1}{({c_{\mathrm{A}}}^{\mathrm{F}} + {c_{\mathrm{B}}}^{\mathrm{F}})} \left(1 + \frac{m_1 + \nu}{m_3 - m_2}\right) \tag{2.20}$$

## 2.5 Design of Linear BP-SMB

For the case of BP-SMB, the user may choose to operate the unit anywhere within the region PQRST, followed by a bypass stream to achieve the target purities. Note that the very fact that the unit can now be operated anywhere within the pentagon improves the robustness of the operation making it amenable to handle variations in feed quality, process disturbances, etc. Apart from the operational flexibility, the goal in this section is to explore if any advantages can be obtained in terms of productivity improvements, and if so, what are the specific conditions at which the BP-SMB can potentially outperform the RP-SMB.

The pentagon can be divided into four regions: Region 1, given by the triangle RSU when both extract and raffinate products from the SMB are 100% pure; Region 2a, given by the triangle QRU where the extract is 100% pure and the raffinate purity is $Pu_{\mathrm{R}}^{\mathrm{tgt}} \leq Pu_{\mathrm{R}}^{\mathrm{SMB}} \leq 100\%$; Region 3a, given by the triangle STU where the raffinate is 100% pure and the extract is $Pu_{\mathrm{E}}^{\mathrm{tgt}} \leq Pu_{\mathrm{E}}^{\mathrm{SMB}} \leq 100\%$; Region 4, given by the rectangular region PQUT where $Pu_{\mathrm{R}}^{\mathrm{tgt}} \leq Pu_{\mathrm{R}}^{\mathrm{SMB}} \leq 100\%$ and $Pu_{\mathrm{E}}^{\mathrm{tgt}} \leq Pu_{\mathrm{E}}^{\mathrm{SMB}} \leq 100\%$.

For the analysis of the BP-SMB (c.f. Fig. 2.1), the steps used for calculating the productivity can be summarized as follows:

1. Fix $m_1$ and $m_4$ to satisfy regeneration constraints.
2. Choose an arbitrary point W ($m_{2,W}$ and $m_{3,W}$) within the Pentagonal region PQRST in Fig. 2.2 such that $Pu_{\mathrm{R}}^{\mathrm{SMB}} \geq Pu_{\mathrm{R}}^{\mathrm{tgt}}$ and $Pu_{\mathrm{E}}^{\mathrm{SMB}} \geq Pu_{\mathrm{E}}^{\mathrm{tgt}}$.
3. Calculate switch time, $t^*$ based on Eq. 2.18.

4. Calculate feed flow rate based on $m_{2,W}$ and $m_{3,W}$ and Eq. 2.10.

5. Use component mass balances to calculate $n_{i,\mathrm{E}}^{\mathrm{SMB}}$ and $n_{i,\mathrm{R}}^{\mathrm{SMB}}$.

6. Calculate bypass volumes $V_{\mathrm{E}}^{\mathrm{BP}}$, $V_{\mathrm{R}}^{\mathrm{BP}}$, using Eqs. 2.7 and 2.8, respectively.

7. Calculate productivity using:

$$Pr^{\mathrm{BP-SMB}} = \frac{V(1-\varepsilon)(m_{3,W} - m_{2,W}) + V_{\mathrm{E}}^{\mathrm{BP}} + V_{\mathrm{R}}^{\mathrm{BP}}}{N_{\mathrm{tot}} V(1-\varepsilon) t^{*,BP-SMB}} (c_A^{\mathrm{F}} + c_B^{\mathrm{F}}) \tag{2.21}$$

8. Calculate desorbent requirement using:

$$DR^{\mathrm{BP-SMB}} = \frac{1}{(c_A^{\mathrm{F}} + c_B^{\mathrm{F}})} \left( 1 + \frac{m_1 V(1-\varepsilon) + V\varepsilon}{(m_3 - m_2)V(1-\varepsilon) + V_{\mathrm{E}}^{\mathrm{BP}} + V_{\mathrm{R}}^{\mathrm{BP}}} \right) \tag{2.22}$$

For the case of RP-SMB, the steps required to calculate the productivity are the same as those described for BP-SMB, except that the operating point must be the one where the purities of the SMB are identical to the target purities and since $V_{\mathrm{R}}^{\mathrm{BP}}$ and $V_{\mathrm{E}}^{\mathrm{BP}} = 0$, the productivity $Pr^{\mathrm{RP-SMB}}$ is obtained from Eq. 2.19.

Using the procedure mentioned above, the ratio of the productivities, denoted as $\Lambda$, achieved by the BP-SMB and RP-SMB in each of the three regions can be calculated. The seemingly complex forms reduce to surprisingly simple equations:

$$\text{Region 2a}: \ \Lambda = \frac{Pr^{\mathrm{BP-SMB}}}{Pr^{\mathrm{RP-SMB}}} = \frac{H_A - m_{2,W}}{H_A - H_B} \frac{t^{*,RP-SMB}}{t^{*,BP-SMB}} \tag{2.23}$$

$$\text{Region 3a}: \ \Lambda = \frac{Pr^{\mathrm{BP-SMB}}}{Pr^{\mathrm{RP-SMB}}} = \frac{m_{3,W} - H_B}{H_A - H_B} \frac{t^{*,RP-SMB}}{t^{*,BP-SMB}} \tag{2.24}$$

$$\text{Region 4}: \ \Lambda = \frac{Pr^{\mathrm{BP-SMB}}}{Pr^{\mathrm{RP-SMB}}} = \frac{t^{*,RP-SMB}}{t^{*,BP-SMB}} \tag{2.25}$$

In Eqs. 2.23 to 2.25, the ratio of switch times for the RP-SMB and BP-SMB play a critical role in determining the ratio of productivities between the two processes, hence it is important to understand how they vary. Equation 2.18 can be written as

$$m_3 = -\frac{N_2}{N_3} m_2 - \left[ \frac{t^* \Delta P_{\max}}{\phi L^2 \varepsilon} - \sum_{j=1}^{4} N_j - \nu(N_1 m_1 + N_4 m_4) \right] \tag{2.26}$$

Once the column configuration, the maximum allowable pressure drop and the values of $m_1$ and $m_4$ are fixed, Eq. 2.26 represents a family of straight lines on the $m_2 - m_3$ plane with a slope of $-N_2/N_3$ with $t^*$ being the varying parameter (see Fig. 2.2). As one moves from the top-right corner of the $m_2 - m_3$ plane to the bottom left, the value of $t^*$ decreases.

Now, let us consider how the productivity ratio will vary in each of the three regions identified above. Note that the point "P" represents the only possible operating condition of the RP-SMB. In Region 2a, by observing that the term $\frac{H_A - m_{2,W}}{H_A - H_B}$ approaches its maximum value of 1 along the line "QU", and the point "U" represents the point which can be operated at the shortest switch time, it is easy to deduce that best productivity is achieved by operating the BP-SMB at point U. Note that operating at U does not guarantee a productivity larger than the RP-SMB, but is the best operating point within region 2a. Similarly it can be shown that point "T" is the best operating condition for both regions 3a and 4. Comparing points T and U, we can deduce that T would offer higher productivity for a simple reason that the switch time corresponding to T will always be shorter than that corresponding to point U. A more detailed analysis of where the BP-SMB will offer higher productivities compared to the RP-SMB can be obtained based on the nature of Eqs. 2.23 to 2.25 and Eqn 2.26. However, from a practical perspective, it would suffice to conclude that point T is the point of interest. In other words, the highest productivity ratio, for the case of an infinitely efficient column, is obtained when the SMB is designed to provide an extract that corresponds to the target purity and the raffinate is pure followed by blending the feed with the raffinate to obtain the target purity. This observation is consistent with the results obtained for single-column bypass chromatography [15]. Summarizing, the maximum ratio of the BP-SMB and RP-SMB productivities (denoted as $\Lambda_{\max}$), operated at points T and P, respectively, is given by:

$$\Lambda_{\max} = \frac{Pr^{\mathrm{BP-SMB,T}}}{Pr^{\mathrm{RP-SMB,P}}} = \frac{\nu(N_1 H_{\mathrm{A}} + N_2 H_{\mathrm{B}}^* + N_3 H_{\mathrm{A}}^* + N_4 H_{\mathrm{B}}) + \sum_{j=1}^{4} N_j}{\nu(N_1 H_{\mathrm{A}} + N_2 H_{\mathrm{B}}^* + N_3 H_{\mathrm{A}} + N_4 H_{\mathrm{B}}) + \sum_{j=1}^{4} N_j} \tag{2.27}$$

which can be rearranged to yield

$$\Lambda_{\max} = 1 + \frac{\nu N_3 (H_{\mathrm{A}}^* - H_{\mathrm{A}})}{\nu(N_1 H_{\mathrm{A}} + N_2 H_{\mathrm{B}}^* + N_3 H_{\mathrm{A}} + N_4 H_{\mathrm{B}}) + \sum_{j=1}^{4} N_j} \tag{2.28}$$

The second term on the RHS of the above equation is always positive and hence the BP-SMB can always be designed to provide a higher (or at least equal) productivity compared to the RP-SMB.

Finally, using a similar approach, for the case where the BP-SMB and RP-SMB are operated with identical $m_1$, it can be shown that the ratio of the desorbent requirements, denoted as $\Theta$, are given by:

$$\text{Region 2a}: \ \Theta = \frac{DR^{\mathrm{BP-SMB}}}{DR^{\mathrm{RP-SMB}}} \geq 1 \tag{2.29}$$

$$\text{Region 3a}: \ \Theta = \frac{DR^{\mathrm{BP-SMB}}}{DR^{\mathrm{RP-SMB}}} \geq 1 \tag{2.30}$$

$$\text{Region 4}: \ \Theta = \frac{DR^{\text{BP-SMB}}}{DR^{\text{RP-SMB}}} = 1 \tag{2.31}$$

These are quite interesting results that show that the BP-SMB does not provide any advantage in terms of solvent consumption. This again is fully consistent with the observations made for bypass-chromatography [15]. Specifically, the desorbent requirement in region 4, where productivity advantages are seen does not disadvantage the BP-SMB in terms of desorbent requirement, while providing the additional possibility to improve productivity.

### 2.5.1 Validation of the linear BP-SMB design

Prior to proceeding with the analysis of the BP-SMB, it is important to confirm that the design equations derived in the previous section are indeed correct. In order to demonstrate this we consider the separation of Tröger's base enantiomers on microcrystalline cellulose acetate [14]. As an aside, there is no specific reason to choose this system, other than the fact that it has been well characterized and used in our previous studies [15]. The adsorption isotherms of the two enantiomers are given by:

$$(+)\text{TB}: q_{\text{A}}^{*} = \frac{6.45 c_{\text{A}}}{1 + 0.39 c_{\text{A}} + 0.065 c_{\text{B}}} \tag{2.32}$$

$$(-)\text{TB}: q_{\text{B}}^{*} = \frac{2.18 c_{\text{B}}}{1 + 0.39 c_{\text{A}} + 0.065 c_{\text{B}}} \tag{2.33}$$

where $c_i$ is the fluid phase concentration in g/L. Under linear conditions, $H_{\text{A}} = 6.45$ and $H_{\text{B}} = 2.18$.

SMB studies can be categorized into two groups: problems that consider the development of new units where column dimensions are to be designed and problems where a given unit is considered as available and the possibilities of improving its performance is analysed. This work focuses on the second class of problems. However, we expect the results to also hold true for the first type of problems. The specific SMB configuration considered is provided in Table 2.1. For this situation, the productivity ratios calculated for target purities using Eqs. 2.23 to 2.25 for $Pu_{\text{R}}^{\text{tgt}} = Pu_{\text{E}}^{\text{tgt}} = 75\%$ are shown in Fig. 2.3 (a). The contours clearly indicate that for this case, certain portions of regions 3a (STU) and 4 (PQUT) where the BP-SMB has a higher productivity compared to RP-SMB. Further, the maximum productivity ratio corresponds, as predicted, to point T. In order to confirm the analytical solutions, numerical simulations were performed using very low values of $D_{\text{L}}$ and a large number of finite volumes. The $m_2 - m_3$ plane was discretized into hundreds of points (shown as dots in Fig. 2.3 (b)). For each of these points, the minimum switch time was calculated using Eq. 2.18 and the SMB was simulated numerically until cyclic steady state was reached. Based on the mass balances, the bypass volumes were calculated which yielded the value of productivity. The productivity ratios obtained from the numerical

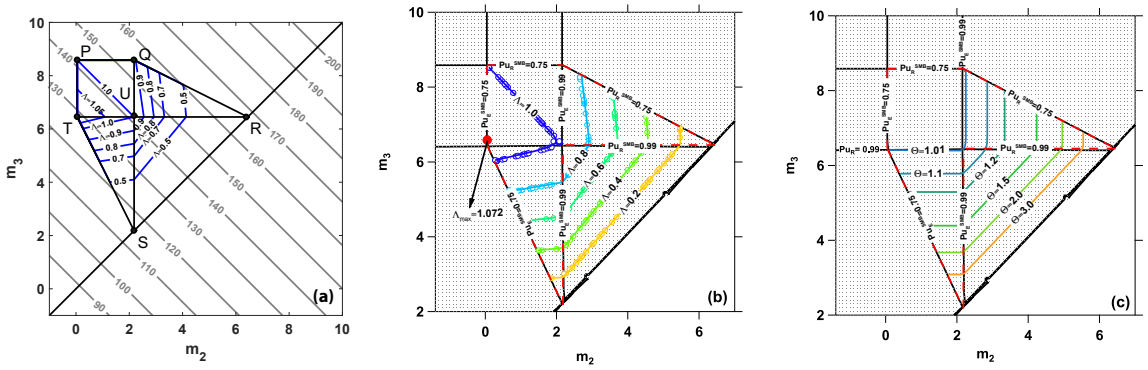


Figure 2.3: Validation of design equations for Linear BP-SMB (a) Contours of productivity ratio, $\Lambda$, for the case of Tröger's base enantiomers under ideal conditions calculated from analytical expressions. The parallel lines for constant $t^*$[s] are plotted for a $\Delta P_{\max} = 40$ bar. The contours are calculated for target extract and raffinate purities of 75%; (b) Comparison between the contours of $\Lambda$ obtained from analytical solutions (separation region represented by red dashed lines and productivity ratio by $\circ$) and from numerical simulations (represented by solid lines); (c) Contours of the ratio of desorbent requirement, $\Theta$, for BP-SMB and RP-SMB calculated from numerical simulations.

simulations (lines) and analytical equations (symbols) are superimposed in Fig. 2.3 (b). The comparison shows the excellent match between the two approaches, thus validating the analytical expressions. Finally, Fig. 2.3 (c) shows the ratio of the desorbent requirements of the BP-SMB and RP-SMB obtained from the numerical simulations. This plot confirms the expectations that, specifically in Region 4, the desorbent requirements for both the BP-SMB and RP-SMB are identical.

### 2.5.2 Analysis of Linear BP-SMB under ideal conditions

Enabled by the derivation of the maximum productivity ratio and confirmation using numerical simulations, it is now possible to analyse conditions under which the BP-SMB provides advantages over the RP-SMB. From Eq. 2.28, it is quite clear that the a number of factors such as the number of columns in each section, the Henry constants, the feed compositions of the two components and the expected target purities influence the choice. In the following analysis, we consider cases where the number of columns in each section of the SMB are identical and that the conditions of $m_1 = H_{\mathrm{A}}$ and $m_4 = H_{\mathrm{B}}$ are imposed. Note that these two conditions provide the lower limits for $m_1$ and $m_4$. Increasing these values will diminish the advantage of the BP-SMB as it can be clearly inferred from Eq. 2.28. For the following three case studies, the base case considered is the separation of a Tröger's base racemic mixture with target purities of 75% for both raffinate and extract.

| Parameter | Tröger's base system | HFCS system |
|---|---|---|
| Column length, $L$ [cm] | 10 | 10 |
| Column diameter, $d$ [cm] | 1 | 1 |
| Column void fraction, $\varepsilon$ | 0.59 | 0.59 |
| Column configuration | 1-1-1-1 | 1-1-1-1 |
| Component feed concentration, $c_i^{\mathrm{F}}$ [g/L] | 3 (A and B) | 465 (glucose) |
| | | 335 (fructose) |
| Axial dispersion coefficient, $D_{L,i,j}/v$ | 3.01 x $10^{-2}$ | 1.00 x $10^{-2}$ |
| Maximum allowed pressure drop, $\Delta \mathrm{P}_{\mathrm{max}}$ [bar] | 40 | 40 |
| Permeability, $\phi$ [bar.s/cm$^2$] | 0.1 | 0.1 |

Table 2.1: Modelling parameters for the case studies considered.

As the first case study, we explore the effect of the target purities on the advantage of a BP-SMB. Figure 2.4 (a) shows the contours of $\Lambda$ as function of the extract and raffinate purity operated at point T. The figure clearly illustrates the fact that the BP-SMB is naturally preferred only when the target extract and raffinate purities are low. It is also interesting to see that the target raffinate purity has a higher impact on $\Lambda$ as compared to the extract purity. For a given extract purity, $\Lambda$ is a strong function of the raffinate purity. However, for a given raffinate purity, $\Lambda$ only weakly depend on the extract purity. In order to illustrate this we consider three unique scenarios that are represented by the blue, black and yellow circles in Fig. 2.4 (a). Since the Henry constants are identical for all of the three scenarios, the pentagons originate from the diagonal at identical values of $H_{\mathrm{A}}$ and $H_{\mathrm{B}}$ (c.f. Fig. 2.4 (b)). Between the blue and yellow points, note that vertices of P and T, the best operating conditions for the RP-SMB and BP-SMB, respectively are closer to each other for the yellow circle. As shown in Eq. 2.25, since $\Lambda$ is proportional to the ratio of the switch times, we obtain lower $\Lambda$ corresponding to the yellow point. However, comparing the blue and black operating points for which the raffinate purities are identical, it is worth noting that the relative positions of P and T for the corresponding pentagons are nearly identical. This results in nearly identical productivity ratios.

As a second case study, the effect of the Henry constant and selectivity is considered. Figure 2.4 (c) shows the contours of $\Lambda$ as a function of $H_{\mathrm{A}}$ and the selectivity, $\alpha = H_{\mathrm{A}}/H_{\mathrm{B}}$). It is clear from the contour plot that the BP-SMB shows an advantage for systems that have high values of $H_{\mathrm{A}}$ and $\alpha$. In order to illustrate the reason for the same, three different conditions are considered as shown by the circles. For each of these cases, the pentagonal region that guarantees the target purities of both purity and recovery are shown in Fig. 2.4 (d). When the $H_{\mathrm{A}}$ is held fixed and the selectivity is lowered (as shown by the location of the purple circle and the corresponding pentagon), the ratio of the switch times corresponding to vertices P and T

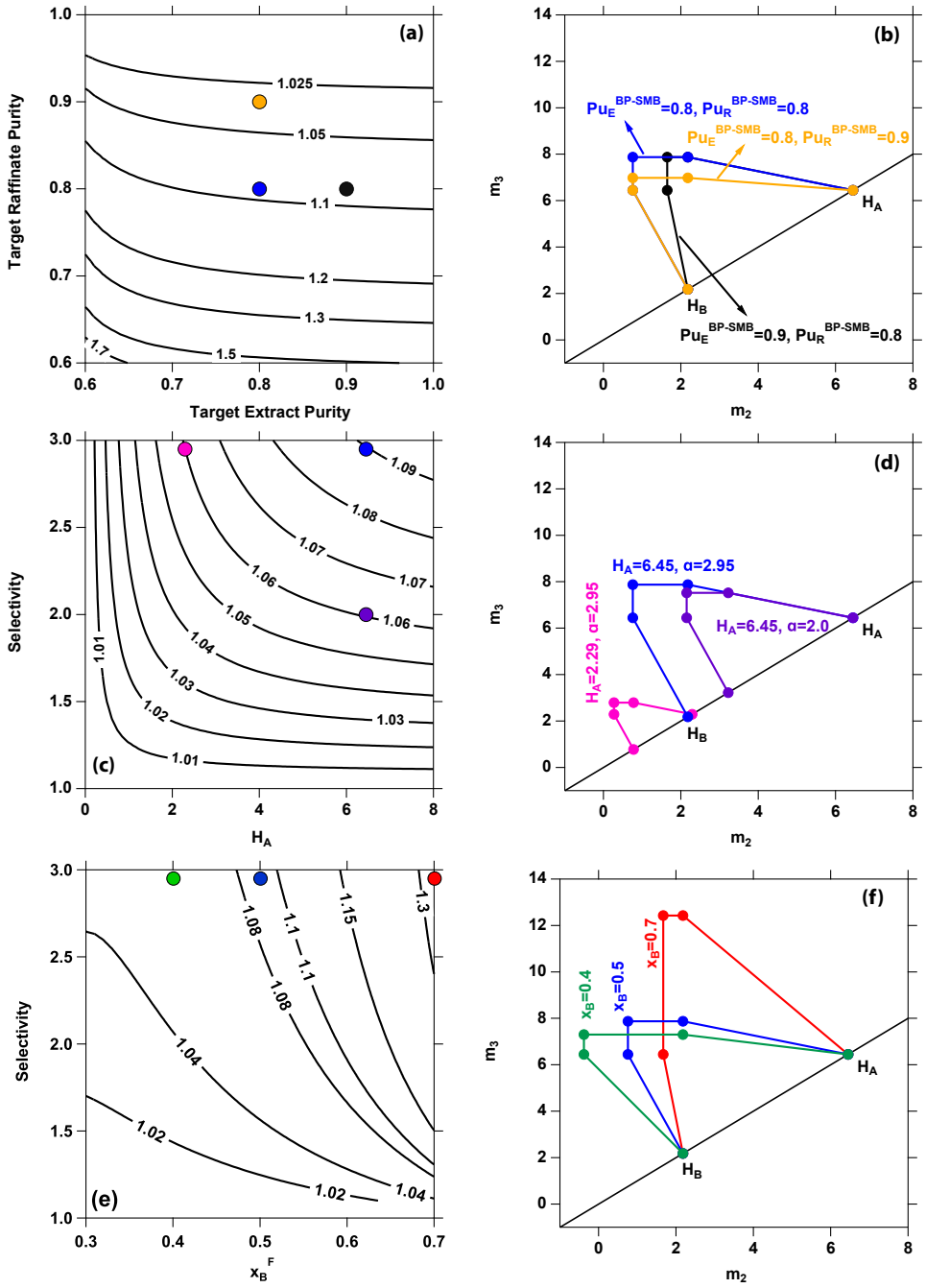


Figure 2.4: Case studies exploring the effect of different parameters on the productivity ratios, Λ. The column of figures on the left represents the contour plots of the productivity ratio, Λ, as a function of two variables listed on the axes. The column on the right shows the separation regions for the operating conditions represented on the contour plot to their left hand side.

of the respective pentagons are of comparable magnitudes but closer in the case of the purple pentagon. This results in a reduction of the productivity. Similarly, when the selectivity is held constant and the value of $H_{\mathrm{A}}$ is reduced (shown by the pink circle and the corresponding pentagon), the position of the pentagon moves to lower values of $m_2$ and $m_3$. First the region where the purities can be guaranteed shrinks and the location of the vertices of P and T are closer to each other. This again results in a lower $\Lambda$.

As a final case study, we consider the effect of the feed composition and selectivity. First we define the solvent-free mole fraction of lighter component as $x_{\mathrm{B}}^F = c_{\mathrm{B}}^F/(c_{\mathrm{A}}^F + c_{\mathrm{B}}^F)$. Hence, when $x_{\mathrm{B}}^F > 0.5$, the feed is rich in the lighter component and richer in the heavier component when $x_{\mathrm{B}}^F < 0.5$. Figure 2.4 (e) shows the impact of $x_{\mathrm{B}}^F$ and the selectivity on the productivity ratio. It can be seen that the BP-SMB is advantageous for systems that are rich in the lighter component. In order to illustrate this, the region of acceptable separation for three different values of $x_{\mathrm{B}}^F$ are shown in Fig. 2.4 (f). It can be seen that for the case of $x_{\mathrm{B}}^F = 0.5$, the pentagon is symmetric (along the axis that is orthogonal to the diagonal and passes through the vertex). In the case of $x_{\mathrm{B}}^F = 0.7$, it is interesting that the pentagon is skewed and the vertices P and T are further separated compared to the case where $x_{\mathrm{B}}^F = 0.4$. This clearly results in a larger $\Lambda$.

Summarizing, the advantages of the BP-SMB over a RP-SMB are clearly seen under the the following conditions: when the feed is rich in the lighter component; the Henry constants of the two components are high; when the selectivity of the system is high; and when low extract and raffinate purities are desired. As shown, significant advantages can be acquired when all these conditions are met.

### 2.5.3 Effect of column efficiency

The pentagonal region delimited by the design equations seen in Fig. 2.2 is a very good starting point when designing a BP-SMB process. However, it is important to notice that this separation region is obtained considering columns with infinite efficiency. Real columns tend to have lower efficiency due to axial dispersion and mass transfer resistances; decreasing the purity of both light and heavy products. Hence, it is important to study the effect of column efficiency on the BP-SMB performance. Since there are no explicit analytical equations to analyse the effect of column efficiency on the performance of a SMB, a numerical approach is adopted. Conservative constraints of $m_1 = 10$ and $m_4 = 0.1$ were adopted to ensure that the regeneration requirements are conveniently met for a wide range of column efficiencies. Then, the $m_2 - m_3$ plane was discretized into hundreds of points and the performance of both the BP-SMB and RP-SMB were calculated for a target purity of $Pu_{\mathrm{R}}^{\mathrm{tgt}} = Pu_{\mathrm{E}}^{\mathrm{tgt}} = 75\%$

In order to study the effect of column efficiency, an entire set of simulations were performed

with the axial dispersion coefficient varying from 3.01x10$^{-4}$ to 3.01x10$^{-1}$ cm$^2$/s. For each value of axial dispersion coefficient, a pulse injection on a single column was simulated to calculate the number of theoretical plates per column. The results of this study are shown in Fig. 2.5 (a), where the maximum productivity ratios and the corresponding product purities (i.e., $Pu_{\mathrm{E}}^{\mathrm{BP-SMB}}$ and $Pu_{\mathrm{R}}^{\mathrm{BP-SMB}}$) are plotted as a function of their respective number of theoretical plates. First, it can be noted that $\Lambda_{\max}$ decreases as the column efficiency drops. At very low values of column efficiency, the analysis shows that there is no productivity advantage to be gained from the BP-SMB. The asymptotic approach of the $\Lambda_{\max}$ curve to the value obtained for an ideal scenario (denoted by the red dashed line and calculated with Eq. 2.28) is another confirmation of the linear design methodology derived in the previous sections.

Figure 2.5 (b) shows the purity of the extract and raffinate from the SMB corresponding to the maximum productivity operating points shown in Fig. 2.5 (a). As the column efficiency increases, the values of the $Pu_{\mathrm{E}}^{\mathrm{BP-SMB}}$ and $Pu_{\mathrm{R}}^{\mathrm{BP-SMB}}$ at which $\Lambda_{\max}$ is attained also approach the expected condition seen in the ideal system. The purity $Pu_{\mathrm{R}}^{\mathrm{BP-SMB}}$, initially close to 95%, drops steadily to the target raffinate purity as the column efficiency decreases. On the other hand, the values of $Pu_{\mathrm{E}}^{\mathrm{BP-SMB}}$ remain close to the extract target purity, unaffected by the axial dispersion coefficient.

In order to illustrate these observations, the cases where the number of theoretical plates are 100.8 and 14.8 are presented in Figs. 2.5 (c) and (d), respectively. By analysing the region of complete separation (represented by the black solid lines with purities of 99%), it is noticeable that it shrinks significantly as the column efficiency drops. However, the pentagon for the reduced purity operations (represented by the solid black lines for 75% purity) from both cases are still relatively close to the ideal system (denoted by the red dashed lines). The most noticeable difference is regarding the contour of 75% raffinate purity for the low efficiency column (c.f., Fig. 2.5 (d) ), where the curve shifts to a lower position, decreasing the operational flexibility and maximum attainable productivity ratios, $\Lambda_{\max}$. The productivity ratio contours are also plotted in Fig. 2.5 (c) and 2.5 (d). From the higher efficiency system, it can be noted that there is a region enclosed between the productivity contour of 1.0 and the contour for 75% purity of extract where the BP-SMB offers improved productivity when compared to the RP-SMB (i.e., $\Lambda > 1.0$). For the case where the number of theoretical plates per column is 14.8, the region is nearly non-existent, implying that the operation of BP-SMB is not efficient from the perspective of productivity increase. In both scenarios, the red circles represent the $m_2$ and $m_3$ values from which the highest productivity ratios ($\Lambda_{\max}$) are attained. It is noticeable that in the lower efficiency case the point moves upward, backing the results seen in Fig. 2.5 (a) since it shows that $Pu_{\mathrm{E}}^{\mathrm{BP-SMB}}$ tends to stay constant but $Pu_{\mathrm{R}}^{\mathrm{BP-SMB}}$ decreases, therefore reducing the productivity ratio.

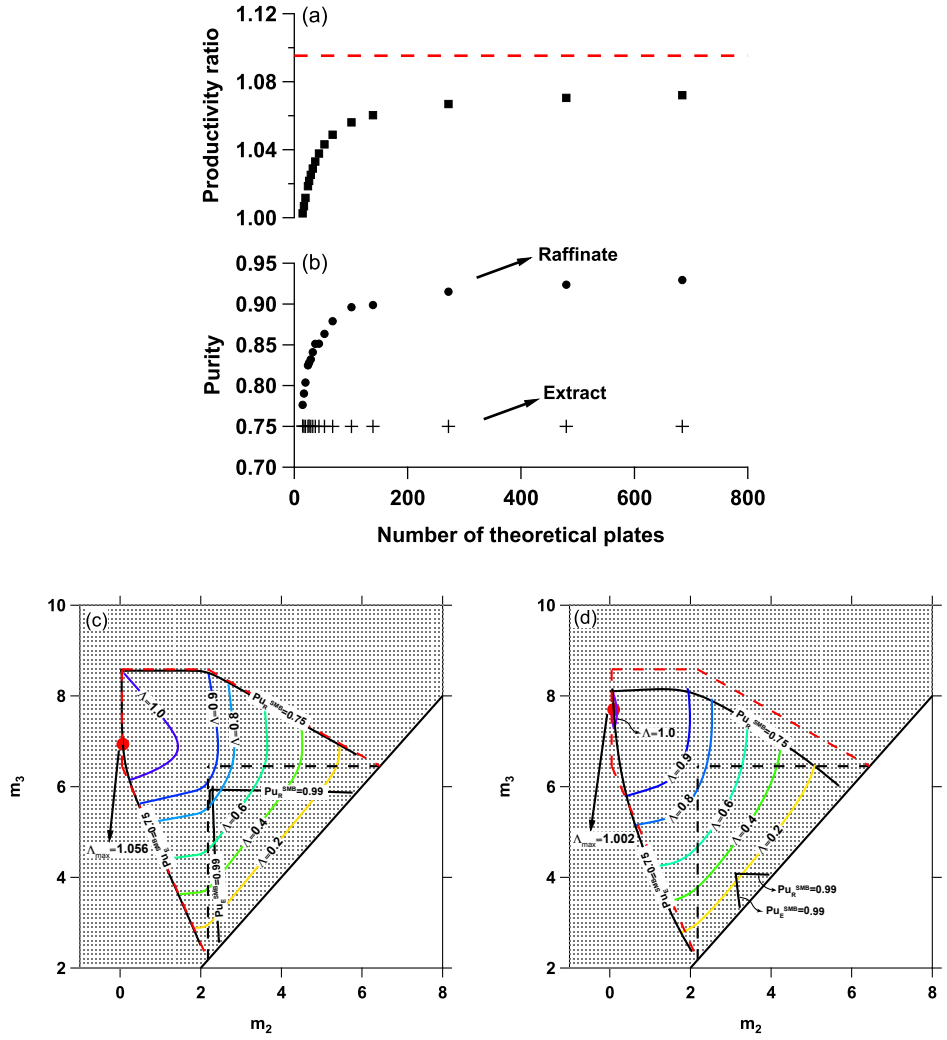


Figure 2.5: Effect of column efficiency on the performance of linear BP-SMB for the separation of a racemic mixture of Tröger's base mixture for 75% pure extract and raffinate under linear equilibrium. (a) Maximum productivity ratio, $\Lambda_{\max}$, and (b) purity of extract and raffinate at optimal operating conditions as a function of column efficiency. Contours of $\Lambda$ and separation region for the cases of (c) number of theoretical plates per column = 100.8 and (d) number of theoretical plates per column = 14.8

## 2.6 Non-linear BP-SMB

In order to analyse the effects of non-linearity in the separation system, the same Tröger's base mixture is considered but now with the competitive Langmuir isotherm. Two scenarios with differing column efficiencies are studied and presented in Fig. 2.6, with numbers of theoretical plates of 100.78 and 14.8. In both cases, the operating region for reduced purity shrinks and skews toward the bottom left corner on the $m_2 - m_3$ plane. Regarding the operating regions for complete separation, it is noticeable in Fig. 2.6 (b) that the area shrinks as the efficiency drops, similar to what was seen for linear systems. However, the region where the reduced purities are obtained is affected to a lesser extent. Considering the region between the productivity ratio contour of 1.0 and the operating lines for reduced purities (i.e., solid black lines), we can conclude that there are advantages in BP-SMB from a productivity perspective in both scenarios. The optimal operating conditions, i.e. red circles, showed again the tendency of higher productivity ratios in regions where $Pu_{\mathrm{E}}^{\mathrm{BP-SMB}} \approx Pu_{\mathrm{E}}^{\mathrm{tgt}}$ and $Pu_{\mathrm{R}}^{\mathrm{BP-SMB}} \geq Pu_{\mathrm{R}}^{\mathrm{tgt}}$.

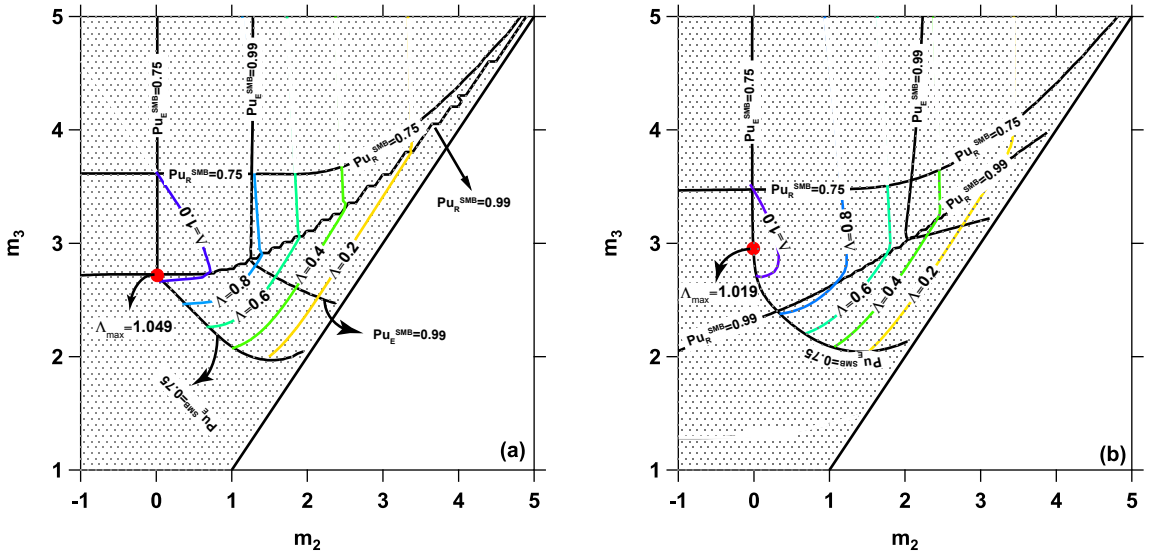


Figure 2.6: Productivity ratio, $\Lambda$, contours and operating regions for non-linear Tröger's base separation for 75% pure extract and raffinate under non-linear conditions with (a) number of theoretical plates per column = 100.8 and (b) number of theoretical plates per column = 14.8. The feed is a racemic mixture with the concentration of each solute being 3 g/L.

### 2.6.1 Effect of feed concentration

To study the effects of feed concentration on the current system, parametric studies were performed by varying the feed concentration from $c_i^F = 0.1$ to $c_i^F = 4.5$ g/L. The maximum productivity ratios achieved in each case are plotted as a function of feed concentration in Fig. 2.7 (a). At low feed concentrations, the productivity ratio first increases; reaches a maximum and

finally drops with further increase in concentration. To analyse this phenomenon in detail, three different case studies were chosen and their respective separation regions are plotted in Fig. 2.7 (b), with the optimal operating condition in each case indicated by their respective circles. The blue boundary represents a system with $c_i^F = 0.3$ g/L and it is noticeable that it resembles the pentagon obtained in linear cases, since the low concentrations reduced the effects of non-linearity in the system. The green and black curves represent a system with $c_i^F = 1.0$ and $c_i^F = 3.0$ g/L, respectively.

As the feed concentration increases, the operating region shrinks and bends toward the bottom left region on the $m_2 - m_3$ plane, going from a symmetric pentagon to the shape seen previously for non-linear systems. On one hand, as seen from the operating regions for $c_i^F = 0.3$ g/L and $c_i^F = 1.0$ g/L, the relative positions of the operating points for RP-SMB and BP-SMB do not change significantly. However, for the case of $c_i^F = 1.0$ g/L, the absolute values of the switch times are lower compared to the case of $c_i^F = 0.3$ g/L, resulting in an increase in $\Lambda_{\max}$. On the other hand, it can be seen that for $c_i^F = 3.0$ g/L the operating points for BP-SMB and RP-SMB are closer to each other when compared to the previous cases. This results in reductions to the values of $\Lambda_{\max}$, explaining the trend seen in Fig. 2.7 (a). It is worth mentioning that for all case studies analysed, $\Lambda_{\max}$ was higher than 1.04, showing the advantages of BP-SMB over RP-SMB from a productivity perspective.

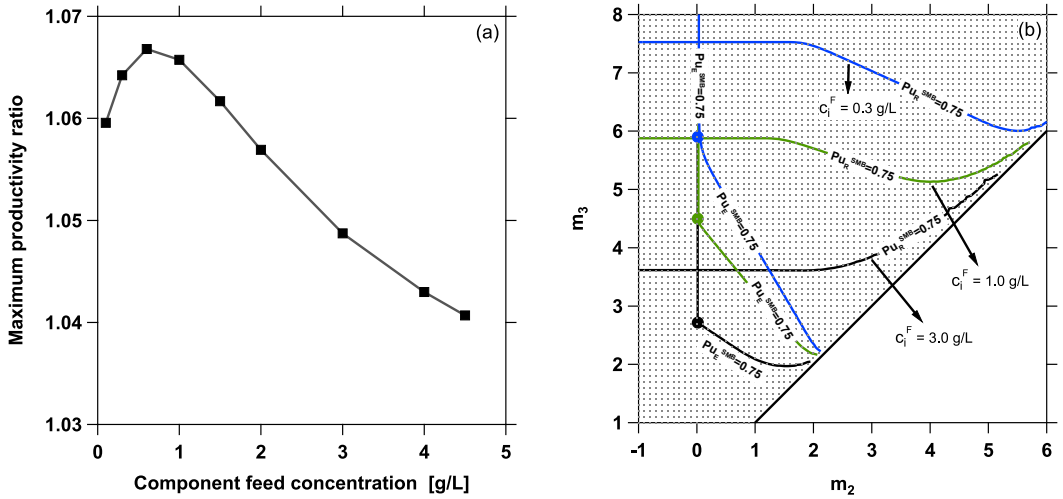


Figure 2.7: Effect of feed concentration on the performance of non-linear BP-SMB for the separation of a racemic feed of Tröger's base enantiomers. (a) Maximum productivity ratio, $\Lambda_{\max}$, as a function of total feed concentration. (b) Operating regions for 75%/75% target purities.

## 2.7 Production of high-fructose corn syrup

One of the practical applications of the BP-SMB is in the production of high fructose corn syrup (HFCS), a sweetener [10]. In terms of quantity of the product manufactured globally, this is one of the largest applications of the SMB technology. The production of HFCS involves the isomerization reaction of glucose that produces a stream that contains 42% fructose and 58% glucose [26, 27]. This stream, called HFCS 42, is fed to a SMB unit that is tasked to separate the glucose (light raffinate product) and the fructose (heavy extract product). The product fructose that is sold in the market consists of 55% fructose and the rest being glucose. This product is called HFCS 55. The raffinate, typically consisting of 90% glucose, is recycled to the isomerization reactor, while the extract is removed as the product. There are two approaches to produce HFCS 55. The first approach, referred to as Process $\alpha$ [10], is to operate the SMB in such a way that the extract product is HFCS 55, i.e. as a RP-SMB. The second approach, referred to as Process $\beta$, is to operate the SMB so that the extract product contains 90% fructose and blend it with HFCS 42 in order to achieve a final product that meets the requirement of HFCS 55, i.e. as a BP-SMB. In fact, it is Process $\beta$ that is used in the industry. Nicoud, using a series of heuristic arguments, shows that the productivity of both approaches are almost the same and the reasons why Process $\beta$ is chosen is based only on operational issues [10]. The two main reasons he cites are the following: 1. Owing to the variation in the feed quality, the incoming feed to the SMB is not strictly 42%. By overpurifying the extract, the operator retains the flexibility to allow for some variation in the product quality that can be tackled easily not by changing the operating conditions of the SMB but by changing amount that is blended. 2. Owing to the low retention factors of both fructose and glucose, Process $\alpha$ would result in a situation where the flow rate in section 2 is very small (nearly zero), while that in section 1 is quite high. This drastic change in the flow rate during a switch can cause physical damage to the stationary phase, which is avoided in Process $\beta$. In this section, we analyze this separation to verify the empirical arguments.

### 2.7.1 Linear - equilibrium theory analysis

Under low concentrations, the equilibrium of fructose and glucose can be described by linear isotherms with the Henry constants being $H_{\text{fr}} = 0.46$ and $H_{\text{gl}} = 0.27$, respectively, resulting in a selectivity of $\alpha = 1.7$ [10]. Noticing from the previous discussions, it is rather obvious that the Henry constants of this system are low, the selectivity is modest and the feed is marginally enriched in the light component. Hence, the advantages of a BP-SMB separation over the RP-SMB can be expected to be rather modest. The operating points for the Processes $\alpha$ and $\beta$, for the case of a unit with infinite efficiency are shown in Fig. 2.8 as $\text{P}_\alpha$ and $\text{P}_\beta$, respectively. A few observations can be immediately made. The region within the pentagon where the BP-SMB

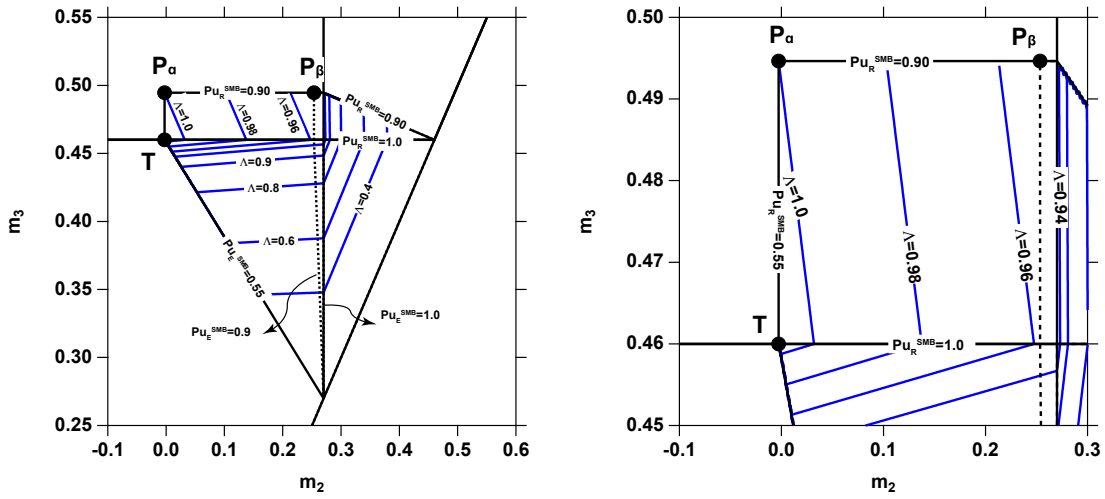


Figure 2.8: Separation region for HFCS 42 under ideal conditions showing the operating points of a RP-SMB ($P_\alpha$) and the BP-SMB ($P_\beta$) as operated in the industry. The lower figure shows the zoom of the region of interest.

proves to be better than the RP-SMB for producing a raffinate containing 90% glucose and an extract containing 55% fructose is very small. The maximum productivity ratio, which can be achieved by operating the SMB at point T and bypassing some feed, even under ideal conditions, is only 1.006. This indicates that operating a BP-SMB at its optimal condition does not offer any advantage even under ideal conditions. The productivity ratio corresponding to the point $P_\beta$ is $\approx 0.95$ indicating that the drop in productivity is about 5% compared to $P_\alpha$. Under ideal conditions, it appears that Process $\alpha$ is advantageous compared to Process $\beta$ using the minimum switch time design.

### 2.7.2 Modelling and simulation for non-ideal and non-linear systems

To extend the analysis of the HFCS 55 production, we now model and simulate the unit considering the equilibrium-dispersive model of chromatography. The parameters used are presented in Table 2.1. To avoid any loss of fructose or glucose in the system, the $m_i$ ratios in regions 1 and 4 are set to $m_1 = 1$ and $m_4 = 0.1$.

For a linear system, the isotherm parameters used are the same as the ones mentioned in the previous section. On the other hand, the isotherm for non-linear systems are described by Eq. 2.34 and 2.35 [10]. The following quadratic equations are fairly non-linear at high concentrations and are expressed in g/L.

$$q_{\mathrm{gl}}{}^{*} = 0.27c_{\mathrm{gl}} + 0.00012{c_{\mathrm{gl}}}^{2} + 0.0001c_{\mathrm{gl}}c_{\mathrm{fr}} \tag{2.34}$$

$$q_{\mathrm{fr}}{}^{*} = 0.46c_{\mathrm{fr}} + 0.00012{c_{\mathrm{fr}}}^{2} + 0.00024c_{\mathrm{fr}}c_{\mathrm{gl}} \tag{2.35}$$

The operating regions, productivity ratio contours and operating points $P_\alpha$ and $P_\beta$ are plotted in Figs. 2.9 (a) and (b). In both linear and non-linear cases, the productivity advantages of BP-SMB are non-existent, as seen by the absence of a productivity ratio contour of 1.0 or higher inside the operating region (e.g., the commonly used route indicated by $P_\beta$ results in a productivity ratio close to 96%). Different from what was observed earlier, operating the SMB unit at the optimal point T indicated by the design methodology (i.e. overpurified raffinate product and extract at target purity) also results in productivity ratio $< 1.0$. A simple case study by limiting the maximum allowed pressure drop to 4 bar, representative of a practical situation was performed and compared to the current results. Although the absolute productivities of both the BP-SMB and RP-SMB dropped, the productivity ratios, $\Lambda$, remained invariant.

For the separation of HFCS 55, even though the feed is richer in glucose (i.e., light product), the added effects of low Henry constants, modest selectivity and high extract purity requirement (when compared to the raffinate product requirement) results in an overall low $\Lambda_{\max}$, therefore, a system where there are no productivity advantages when using BP-SMB. This analysis confirms Nicoud's observations that the main advantage of using a BP-SMB for HFCS production is purely based on operational advantages rather than any economic benefits.

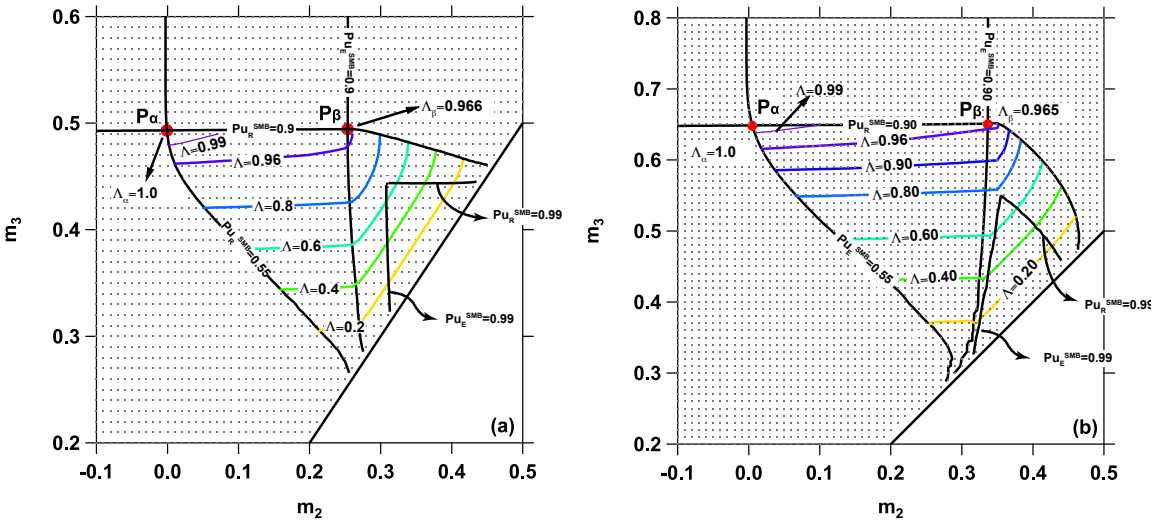


Figure 2.9: HFCS 42 operating region with different target purities (90%/55%, 90%/90% and 99%/99% for raffinate and extract target purities, respectively). Productivity ratio contours are presented for both (a) linear isotherm and (b) non-linear isotherm systems.

## 2.8 Conclusions

A methodology to design and evaluate RP-SMB and BP-SMB based on the equilibrium theory analysis was presented. The first key observation is the fact that there is one unique operating

condition where the SMB can be designed to produce purities that are lower than 100%. This inherently makes the SMB non-robust for reduced purity requirements. Since the BP-SMB allows for overpurification of the products from the SMB while retaining the option of bypassing the feed, it significantly improves the robustness of the process. The second observation, which resulted from a thorough analysis, is that it is possible to design the BP-SMB to be more productive without increasing the desorbent requirement, compared to the RP-SMB. The results showed that high productivities in BP-SMB are attainable when the feed is richer in the light component, the Henry constants and selectivity are high and when low extract and raffinate purities are desired. Numerical simulations for both linear and non-linear systems validated the methodology and showed the effects of lowering column efficiency on the operating region and process performance. Low column efficiencies tend to decrease the maximum productivity and productivity ratio attainable. The optimal operating conditions are generally obtained when the extract product is close to the target purity and the raffinate product is overpurified. The results obtained for the HFCS 55 purification from both the equilibrium theory analysis and numerical simulations supported the conclusions reached by Nicoud [10] in which BP-SMB do not provide productivity advantages over RP-SMB when purifying fructose; the main advantages are due to the improved robustness offered by the BP-SMB.

# Chapter 3

# Improving the performance of VSA based $CO_2$ capture for reduced recovery requirements [1]

## 3.1 Introduction

The global scientific community is in consensus over the cause of and the ill effects of man-made climate change [28, 29]. Various technologies have been proposed to tackle this problem via reduction of anthropogenic greenhouse gas emissions. While many of these technologies rely on switching to renewable energy sources and the development of more efficient ways of using energy, there needs to be a way to transition our ever growing fossil fuel-based energy infrastructure in a sustainable manner [30]. Carbon capture and sequestration (CCS) is one technique that can create significant reduction of $CO_2$ emissions by capturing and storing $CO_2$ while enabling a smoother transition to a sustainable future [31, 32].

Post combustion $CO_2$ capture (PCCC) is a technique where $CO_2$ is separated from the flue gas stream at the outlet of a fossil fuel based power plant, following the combustion of the fuel [33]. In the case of coal based power plants, the flue gas mixture is generally a very dilute stream (12-15 mol% $CO_2$) and is at near atmospheric conditions of pressure and temperatures [1, 34–36]. The main goal is to concentrate this dilute stream to one that has a $CO_2$ purity in excess of 95%. The stipulated product purity is required due to aspects of transportation and storage of $CO_2$ in underground facilities and/or for enhanced oil recovery (EOR) [37].

[1] This chapter will be submitted for publication as R. T. Maruyama, K. N. Pai, S. G. Subraveti and A. Rajendran, "Improving the performance of VSA based $CO_2$ capture for reduced recovery requirements: doing more by doing less".

Large PCCC demonstration projects are being set-up and some are running and capturing large amounts of $CO_2$ [5]. The most common technology used industrially for this separation is liquid absorption [32,38]. The cost of $CO_2$ captured using liquid amines is considered to be high, hence, alternative separation techniques are being explored [39]. Adsorption based processes, have been studied as an alternative to the liquid absorption process for $CO_2$ capture [33, 40–42]. Detailed numerical studies and experimental demonstration at various scales have been reported [6, 43]. However, advancement and implementation of this technology and others have been slower than expected. A major reason for this arises from the high cost of capture, complexity of the process and other factors.

The goal of any $CO_2$ capture technology is to concentrate the dilute $CO_2$ to a high purity at the lowest cost. Two main constraints are often considered in $CO_2$ capture studies, namely product purity and recovery. The $CO_2$ purity refers to the mole fraction of $CO_2$ in the product stream. This constraint is dictated by downstream requirements and is usually considered a hard constraint. The $CO_2$ recovery refers to the ratio of the amount of $CO_2$ in the product stream to that in the feed stream. Several studies have considered a minimum recovery of at least 90% [44]. While we have been unable to find a document that explicitly mentions this number, many U.S. Department of Energy benchmark studies and solicitations are performed for the case of 90% capture. While we have not been able to identify the rationale for this, one could argue that the high recovery constraint will favor technologies that have bigger impact on large-scale mitigation strategies. In the same vein, it could be also argued that setting high recovery requirements could prevent the exploration of other novel technologies that can prove to be cost effective. As an aside, it is worth pointing out that post-combustion capture, differs from pre-combustion capture. In pre-combustion capture, i.e. the separation of a $CO_2/H_2$ mixture, the objectives are two-fold: generation of high purity $CO_2$ and $H_2$. Both these objectives require the simultaneous achievement of high purity and recovery of $CO_2$. However, in the case of post-combustion capture, the other components (primarily $N_2$) have no downstream use, hence, the sole purpose is to produce high purity $CO_2$. Under these conditions, it is pertinent to consider partial recovery scenarios for post-combustion $CO_2$ capture.

In a recent publication, the National Energy Technology Laboratory (NETL) studied the sensitivity of capture rates on coal power plants performance [44]. The report concluded that in most cases, the reduction in recovery targets decreased the cost of electricity (COE), mainly due to a reduction in capital and operational expenditure. However, the cost of $CO_2$ captured decreased with increasing capture rates. This was possible due to the economy of scale achievable by the use of larger equipment. One of the important conclusions of the report was that lower capture rates allows for more real world demonstration and can aid in scaling up and the optimization of $CO_2$ capture systems. This can retroactively help understand the advantages and limitations of

the various $CO_2$ capture technologies. It was also concluded that this approach of partial recoveries will enable for a smooth progression from a process perspective, while enabling the capture of large amounts of emitted $CO_2$ which would have been left un-captured due to economical reasons.

The goal of the current work is to study the impact of $CO_2$ lower recovery constraint on vacuum swing adsorption (VSA) based capture of $CO_2$ from dry post-combustion flue gas. In this paper, detailed process simulations are performed using a Finite Volume Method (FVM) based PVSA code developed in-house [1] and it is coupled with a genetic algorithm (NSGA-2) [45] for multi-objective optimization of the performance indicators. The effect of reduced capture rates was also studied for multiple solid adsorbents. The impact of varying vacuum pump efficiency was tested along with different flue gas compositions typically observed in industrial environments.

## 3.2 Process design and modeling

### 3.2.1 Adsorbent selection

In order to expand the analysis of reduced $CO_2$ recovery in VSA cycles, four different solid adsorbents are considered for the simulations: Zeolite 13X (Z10-02) [43], UTSA-16 [46], a type of activated carbon (CS-AC) [47] and the Lowest Energy Isotherm Material, which is a theoretical adsorbent obtained *in silico* from a multi-objective optimization procedure that minimizes energy consumption for VSA-based $CO_2$ capture [48]. Zeolite 13X is a well studied adsorbent and current benchmark material for $CO_2$ capture. UTSA-16, a type of metal-organic framework (MOF), is a material that was found to be a very low energy consuming adsorbent in many recent PSA studies [49]. Activated carbon is a well known adsorbent used in different separation processes including gas separation and purification. Its hydrophobic properties and relatively low production costs make it a potential candidate in reduced recovery scenarios.

In these cases, a dual-site Langmuir (DSL) model, which is an extension of the single-site Langmuir (SSL) isotherm equation, is used:

$$q_i^* = \frac{q_{\mathrm{sb},i} b_i c_i}{1 + \Sigma b_i c_i} + \frac{q_{\mathrm{sd},i} d_i c_i}{1 + \Sigma d_i c_i} \tag{3.1}$$

where $q_i^*$ is the solid equilibrium loading, $c_i$ is the fluid phase concentration of component $i$, $q_{\mathrm{sb},i}$ and $q_{\mathrm{sd},i}$ are the solid phase saturation capacities, $b_i$ and $d_i$ are the affinity parameters for the two sites. The temperature dependence is described by the following relationships:

$$b_i = b_{0,i} e^{-\Delta U_{\mathrm{b},i}/RT} \tag{3.2}$$

$$d_i = d_{0,i} e^{-\Delta U_{\mathrm{d},i}/RT} \tag{3.3}$$

where $b_{0,i}$ and $d_{0,i}$ are the pre-exponential factors, while $\Delta U_{\mathrm{b},i}$ and $\Delta U_{\mathrm{d},i}$ are the internal energies. In summary, the DSL isotherm model has 6 parameters, namely, $b_{0,i}$, $d_{0,i}$, $\Delta U_{\mathrm{b},i}$, $\Delta U_{\mathrm{d},i}$, $q_{\mathrm{sd},i}$, and $q_{\mathrm{sb},i}$. The physical properties and isotherm parameters from the adsorbents can be found in Tables 3.1 and 3.2, respectively.

| | |
|---|---|
| Bed length, $L$ [m] | 1.0 |
| Column inner radius, $r_{\mathrm{in}}$ [cm] | 14.45 |
| Column outer radius, $r_{\mathrm{out}}$ [cm] | 16.20 |
| Bed voidage, $\varepsilon$ [-] | 0.41[1]; 0.37[2,3,4] |
| Particle voidage, $\varepsilon_{\mathrm{p}}$ [-] | 0.35 |
| Particle radius, $r_{\mathrm{p}}$ [mm] | 0.750 |
| Tortuosity factor, $\tau$ [-] | 3.0 |
| Density of the solid particle, $\rho_{\mathrm{p}}$ [kg/m$^3$] | 1,130[1,3]; 1680.0[2]; 799.50[4] |
| Density of the column wall, $\rho_{\mathrm{s}}$ [kg/m$^3$] | 7,800 |
| Effective heat conduction coefficient, $K_{\mathrm{z}}$ [J/m/s/K] | 0.0903 |
| Thermal conductivity of the wall, $K_{\mathrm{w}}$ [W/m/K] | 16.0 |
| Inside heat transfer coefficient, $h_{\mathrm{in}}$ [W/m$^2$/K] | 8.6 |
| Outer heat transfer coefficient, $h_{\mathrm{out}}$ [W/m$^2$/K] | 10.0 |
| Gas specific heat capacity, $C_{\mathrm{p,g}}$ [J/kg/K] | 1,010.6 |
| Adsorbent specific heat capacity, $C_{\mathrm{p,s}}$ [J/kg/K] | 900.0[1]; 1070.0[2,3,4] |
| Wall specific heat capacity, $C_{\mathrm{p,w}}$ [J/kg/K] | 502.0 |
| Adsorbed phase specific heat capacity, $\mathrm{C_{p,a}}$ [J/kg/K] | 502.0 |
| Fluid viscosity, $\mu$ [kg/m/s] | $1.72\times10^{-5}$ |
| Molecular diffusivity, $D_{\mathrm{m}}$ [m$^2$/s] | $1.60\times10^{-5}$ |
| Adiabatic constant, $\gamma$ [-] | 1.4 |
| Ambient temperature, $T_{\mathrm{a}}$ [K] | 297.15 |
| Feed temperature, $T_{\mathrm{f}}$ [K] | 297.15 |
| Universal gas constant, $R$ [m$^3$Pa/mol/K] | 8.314 |
| Compression/evacuation pump efficiency, $\eta$ [-] | 0.72 |

[1]Zeolite 13X; [2]UTSA-16; [3]Lowest Isotherm material; [4]CS-AC

Table 3.1: Parameters used for simulation

| Gas | Parameters | Zeolite 13X | UTSA-16 | Lowest Energy Isotherm material | Activated carbon |
|---|---|---|---|---|---|
| $CO_2$ | $b_o$ [$m^3$/mol] | $3.93\times10^{-7}$ | $6.24\times10^{-7}$ | $6.90\times10^{-9}$ | $9.40\times10^{-6}$ |
| | $d_o$ [$m^3$/mol] | $1.256\times10^{-7}$ | $1.87\times10^{-23}$ | $5.93\times10^{-4}$ | $1.04\times10^{-5}$ |
| | $\Delta U_1$ [J/mol] | -40,981 | -30,600 | -36,641 | -25,611 |
| | $\Delta U_2$ [J/mol] | -34,188 | -44,700 | -35,690 | -17,551 |
| | $q_{S1}$ [mol/kg] | 2.768 | 5.0 | 4.43 | 0.59 |
| | $q_{S2}$ [mol/kg] | 2.758 | 3.0 | $6.19\times10^{-3}$ | 7.51 |
| $N_2$ | $b_o$ [$m^3$/mol] | $3.134\times10^{-6}$ | $2.96\times10^{-6}$ | $3.13\times10^{-8}$ | $1.81\times10^{-3}$ |
| | $d_o$ [$m^3$/mol] | $3.134\times10^{-6}$ | 0.0 | $3.13\times10^{-8}$ | $1.72\times10^{-12}$ |
| | $\Delta U_1$ [J/mol] | -15,715 | -9,770 | -15,800 | -8,673 |
| | $\Delta U_2$ [J/mol] | -15,715 | 0.0 | -15,800 | -44,903 |
| | $q_{S1}$ [mol/kg] | 2.768 | 12.7 | 4.43 | 0.16 |
| | $q_{S2}$ [mol/kg] | 2.758 | 0.0 | $6.19\times10^{-3}$ | 41.30 |

Table 3.2: Dual-site Langmuir isotherm parameters for $CO_2$ and $N_2$

### 3.2.2 Cycle configuration

In this study, the four-step VSA cycle with light product pressurization (LPP) is employed. The cycle is composed of four steps, including a high pressure adsorption at atmospheric conditions, a co-current blowdown from 1 atm to an intermediate pressure ($P_{int}$), a counter-current evacuation where the pressure is further reduced to low pressures ($P_{low}$) and a repressurization with the light product. The cycle is illustrated in Fig. 3.1. The 4-step VSA cycle with LPP has been demonstrated at pilot-scale and is known to favor low energy consumption over high productivity [50]. The cycle is relatively simple, however, in order to achieve high $CO_2$ purity and recovery, low vacuum pressures are typically required [48].

### 3.2.3 System modeling and optimization

The mathematical model adopted in this work was previously presented and thoroughly tested by *Haghpanah et al.* [1] More details about the constitutive equations (i.e. mass, energy and momentum balances) used to model the system and the boundary conditions can be found in the Supporting Information section.

For practical reasons, the assumptions considered in the model are presented below:

1. Ideal gas law describes the gas phase;
2. Plug flow model with no concentration, temperature or pressure gradients in the radial

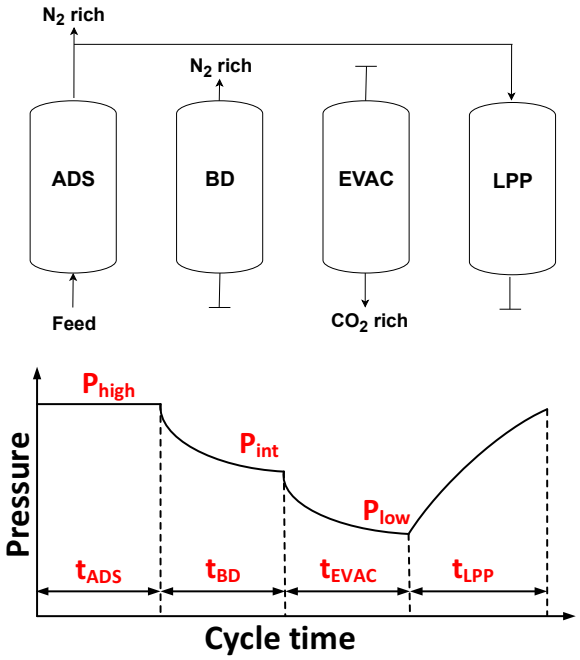


Figure 3.1: 4-step cycle with light product pressurization used for process simulation.

direction;

3. Instant thermal equilibrium between the solid and fluid phase;
4. Linear driving force (LDF) model describes the solid phase mass transfer and the mass transfer resistance is controlled by molecular diffusion in the macropores;
5. The adsorbent properties and bed voidage are uniform throughout the column;
6. Darcy's law describes the column's pressure drop since the equipment dimensions and feed velocities are within the range where Ergun's equation is not required;
7. The outer surface of the column is at constant temperature.

In order to solve this system of partial differential equations (PDE), a finite volume method was used to spatially discretized the adsorption column into 30 control volumes, while the resulting ordinary differential equations were solved simultaneously using the built-in MATLAB solver *ode23s*. The simulations ran for a minimum of 30 cycles and until the mass balance errors were smaller than 0.5%, from which we considered that cyclic steady was reached.

The product purity and recovery of $CO_2$ are process constraints and are defined as:

$$\text{Purity, } Pu_{CO_2}[\%] = \frac{n_{CO_2}^{EVAC}}{n_{total}^{EVAC}} \times 100 \tag{3.4}$$

$$\text{Recovery, } Re_{CO_2}[\%] = \frac{\text{n}_{CO_2}^{EVAC}}{\text{n}_{CO_2}^{feed}} \times 100 \tag{3.5}$$

where $n_i^j$ is the moles of component $i$ collected/fed in step $j$. Energy consumption, which is indicative of the operational cost, is defined as the electrical energy equivalent required to capture one tonne of $CO_2$ from the flue gas.

$$\text{Energy, } En \left[\frac{\text{kWh}_\text{e}}{\text{tonne CO}_2 \text{ captured}}\right] = \frac{E_{ADS} + E_{BLO} + E_{EVAC}}{\text{n}_{CO_2}^{EVAC}} \tag{3.6}$$

In the above expression, $E_{ADS}$ is the energy spent in overcoming the pressure drop during the adsorption step. The terms $E_{BLO}$ and $E_{EVAC}$ refer to the energy consumption in the co-current blowdown and counter-current evacuation steps, respectively. These are calculated as:

$$E_{step}\ [\text{kWh}_\text{e}] = \frac{1}{\eta}\frac{\gamma}{\gamma - 1}\int_{t=0}^{t=t_{step}} (QP)\left[\left(\frac{1}{P}\right)^{\frac{\gamma-1}{\gamma}} - 1\right] dt \tag{3.7}$$

In these equations, $\eta$ represents the efficiency of the vacuum pumps, $\gamma$ is the adiabatic constant, $P$ is the pressure and $Q$ is the volumetric flow rate. The vacuum pump efficiency is an important factor to consider. Most theoretical studies in the literature have assumed values of $\eta$ between 70% and 80% [1,48,49]. However, pilot-scale experiments indicate that vacuum pump efficiency typically drops to $\eta \approx$30%, when low pressures are required [40]. In this paper, we assume $\eta$=72% to be consistent with other literature reports. However, since this is an important issue, a separate case study where efficiency is made a function of the pressure is also considered. Process productivity is another indication of the capital cost and it is defined as:

$$\text{Productivity, } Pr \left[\frac{\text{mol CO}_2}{\text{m}_{\text{adsorbent}}^3 \text{ s}}\right] = \frac{\text{n}_{CO_2}^{EVAC}}{(\text{ Volume of adsorbent }) (\text{Cycle time})} \tag{3.8}$$

The cycle time in the denominator of Eq. 3.8 is the sum of the duration of the different steps in the cycle. It is important to notice that the process productivity will reduce when idle times are added in-between cycle steps to achieve continuous operation. The simulation parameters are provided in Table 3.1.

### 3.2.4 Multi-objective optimization

In order to demonstrate the effects of reduced $CO_2$ recovery, it is not sufficient to consider only parametric studies. Instead, the process needs to be thoroughly optimized. In this work, three different two-objective optimization problems are considered:

1. Maximization of $CO_2$ recovery and minimization of energy consumption;

2. Maximization of $CO_2$ recovery and maximization of productivity;

3. Maximization of productivity and minimization of energy, with $CO_2$ recovery as a constraint.

In all three cases, a constraint of $CO_2$ purity of 95% is enforced. The first two problems give the complete picture of the achievable limits of energy and productivity for different values of $CO_2$ recovery. The third problem provides the trade-off between the performance indicators that eventually decide the operating and capital costs involved. Since all three problems have two conflicting objectives, they result in Pareto fronts. The constraint for purity and recovery (in the case of problem 3) are incorporated by using penalty functions as described in our previous studies [49].

Genetic algorithm based optimization, a well-established tool, was the chosen method to optimize the VSA process. Six decision variables were considered during the multi-objective optimization: adsorption time ($t_{\text{ads}}$), blowdown time ($t_{\text{bd}}$), evacuation time ($t_{\text{evac}}$), intermediate pressure ($P_{\text{int}}$), low pressure ($P_{\text{low}}$) and feed velocity ($v_0$). Their upper and lower boundaries are as follows: $t_{\text{ads}}$=20-300 s, $t_{\text{bd}}$=30-350 s, $t_{\text{evac}}$=30-350 s, $P_{\text{int}}$=0.012-0.950 atm, $P_{\text{low}}$=0.01-0.10 atm and $v_0$=0.1-2.5 m/s. The population size was kept at 144, running for at least 40 generations. It is worth pointing out that the capability of the optimization approach was recently validated experimentally [43].

## 3.3 Results and Discussion

### 3.3.1 Impact of $CO_2$ recovery on process performance

The first case study deals with the impact of $CO_2$ recovery on a process utilizing Zeolite 13X with 15 mol% of $CO_2$ in the feed. The maximization of recovery and minimization of energy was considered, with the low pressure ($P_{\text{low}}$) as one of the decision variables.

Figure 3.2 (a) shows the Pareto curve for the maximization of recovery and minimization of energy consumption (i.e. represented by the black markers). The result clearly indicates that the energy decreases with lower recovery constraints. The effect is more significant at high values of recovery and rather modest at lower values. For instance, reducing the recovery constraint from $Re_{CO_2}$=90% to $Re_{CO_2}$=70% reduces the energy consumption by 27%. However, relaxing the constraint from $Re_{CO_2}$=70% to $Re_{CO_2}$=50% reduces the energy only by 7%. The decision variables corresponding to the Pareto curve are shown in Fig. 3.2 (b), where three key variables are plotted. The value of $P_{\text{low}}$ increases as the recovery constraint is relaxed. $P_{\text{int}}$ followed a similar trend but the value tapered off at low recoveries. These indicate that it is possible to operate the unit at higher pressures when lower recoveries are targeted. The plot of $t_{\text{ADS}} \times v_0$,

which is indicative of the bed utilization, showed a similar trend as $P_{\text{int}}$. The plot of $t_{\text{ADS}} \times v_0$ clearly indicates that bed utilization increases at lower recoveries. In order to understand the reason for the reduction in energy for lower recoveries, it is important to consider the contribution of each step in the cycle, as shown in Fig. 3.2 (c). The breakdown shows that the evacuation step is clearly the biggest contributor to the energy consumption at any given recovery. By lowering the recovery constraint, the contributions from the blowdown and evacuation steps presented a reduction. The evacuation step showed a more contrasting difference when compared to the blowdown step. This is nicely correlated to the observation in Fig. 3.2 (b), where both $P_{\text{int}}$ and $P_{\text{low}}$ increased with lowering recovery. Hence, it can be seen that the main impact on the energy arises from the ability to operate at higher $P_{\text{low}}$.

At this point, it is worth considering once again the Pareto front in Fig. 3.2 (a). Interestingly, the curve did not show recovery values below $Re_{\text{CO}_2}\approx$50%, although there was sufficient room to increase $P_{\text{low}}$ beyond 0.06 atm (note that the upper bound for $P_{\text{low}}$ is 0.10 atm). In order to confirm that this was not due to the inability of the optimizer to find suitable operating conditions, a series of confirmatory tests were performed. In these tests, the low pressure was fixed at different values (i.e. 0.01, 0.03, 0.05, 0.07, 0.085 and 0.10 atm). The optimization routine was repeated for each of these cases and the Pareto fronts are shown along with the case where $P_{\text{low}}$ was a decision variable in Fig. 3.2 (a). The results for $P_{\text{low}}$=0.01, 0.03 and 0.05 atm nicely overlap with the varying $P_{\text{low}}$ Pareto (i.e. black curve), confirming the reliability of the optimization procedure. However, when $P_{\text{low}}$ increased beyond 0.05 atm, the Pareto curves started moving towards the top left region of the plot, indicating that increasing $P_{\text{low}}$ above 0.06 atm in fact is counter productive. It is important to recollect that these optimization results were expected to meet the purity constraint of $Pu_{\text{CO}_2} \geqslant 95\%$. Increasing the vacuum pressure beyond $P_{\text{low}}$=0.06 atm, makes it challenging to achieve the target purity, therefore, in order to meet this constraint, the energy consumption is sacrificed and the working capacity of the sorbent is drastically reduced. The results showed that for the 4-step cycle with LPP, a low pressure of $P_{\text{low}}$ $\approx$0.06 atm is required to achieve the target without adversely affecting the energy consumption. While it is possible to meet the purity constraint for $P_{\text{low}} > 0.06$ atm, it does not serve to improve the process performance.

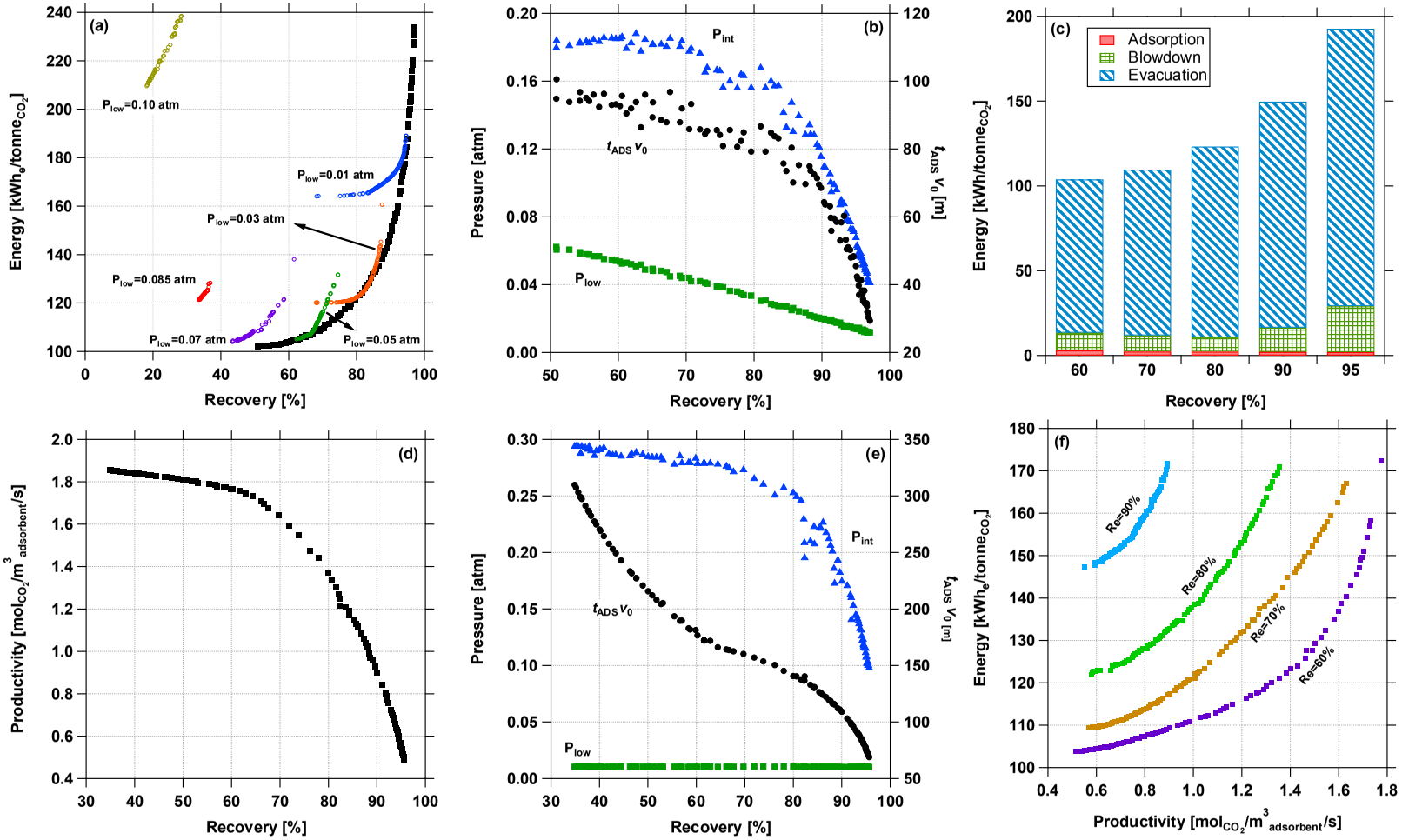


Figure 3.2: Impact of reduced $CO_2$ recovery on the 4-step PSA cycle with Zeolite 13X. (a) Pareto resulting from multi-objective optimization minimizing energy and maximizing recovery are presented for two different cases: (○) fixed low pressures and (■) low pressure as a decision variable. (b) Decision variables corresponding to the Pareto curve shown in sub-figure (a). (c) The energy consumption for each step (i.e. adsorption, blowdown and evacuation) for four points on the Pareto curve in sub-figure (a), each with a different value of $CO_2$ recovery. (d) Pareto curve from multi-objective optimization with maximum productivity and maximum recovery as objective functions. (e) Decision variables corresponding to the Pareto curve shown in sub-figure (b). (f) Pareto curves for the energy-productivity optimization with fixed recovery values.

The effects of reduced $CO_2$ recovery on productivity, our second performance indicator, is shown in Fig 3.2 (d). It is interesting to notice that it presents a similar trend as seen previously in the energy-recovery optimization, where substantial productivity advantages are gained by lowering recovery targets at high recoveries (i.e. reducing recovery from $Re_{CO_2}$=90% to $Re_{CO_2}$=70% results in a productivity increase of 82%), followed by more moderate improvements after that. In order to analyze this phenomenon, four points from the Pareto curve (i.e. operating conditions for $Re_{CO_2}$=90%, 80%, 70% and 60%) were picked and their productivity and solid concentration profiles were analyzed. The solid phase concentration profiles of $CO_2$ per volume of adsorbent throughout the dimensionless column length can be seen in Fig. 3.3. The profiles represent the concentrations at the end of each step in the 4-step VSA cycle and the shaded region represents the area between the blowdown and evacuation profiles, which indicates the amount of $CO_2$ extracted per mass of solid adsorbent. At 90% recovery, due to its high recovery constraint, the $CO_2$ front only advances to $\approx$ 70% of the total column's length during the adsorption step. This way, it avoids loss of $CO_2$ in the adsorption step, however, it results in a low bed utilization. It can be clearly observed that a reduction in the recovery constraint is followed by an increase in bed utilization, where at $Re_{CO_2}$=70% and $Re_{CO_2}$=60% the $CO_2$ front reaches the end of the column. It is worth noting that at these recovery values, the profiles look nearly identical, indicating that the $CO_2$ loss occurs mainly in the adsorption step, leading to a flat productivity value at lower recovery targets.

Considering that the process is unlikely to operate either at the minimum energy consumption or at the maximum productivity operating conditions, Pareto curves for energy-productivity with fixed recovery targets are also provided in Fig. 3.2 (f). The distance between the Pareto fronts is another way to view the advantages of reduced recovery. We can clearly see that the distance between $Re_{CO_2}$=90% and $Re_{CO_2}$=80% is larger than the distance between $Re_{CO_2}$=70% and $Re_{CO_2}$=60% for example, which translates into the exponential Pareto curves seen previously, where energy consumption and productivity were highly impacted with recovery reductions at high recovery values. This plot also indicates that for an energy consumption of 145 $kWh_e/tonne_{CO_2}$, the productivity of the separation unit can be increased by approximately 300% by relaxing the recovery constraint from 90% to 60%. This result exemplifies the impact of reduced recovery requirements.

### 3.3.2 Impact of feed composition

Up to this point, we have been working with a feed composition of 15% $CO_2$ and $N_2$ as balance. This composition is a good estimate in a scenario where CCS is working with dry flue gas from coal-based power plants. In this section, a feed composition of $y_{CO_2}$=0.08 and $y_{CO_2}$=0.20 are also considered, where the first is a good representative of flue gas originated from the combustion

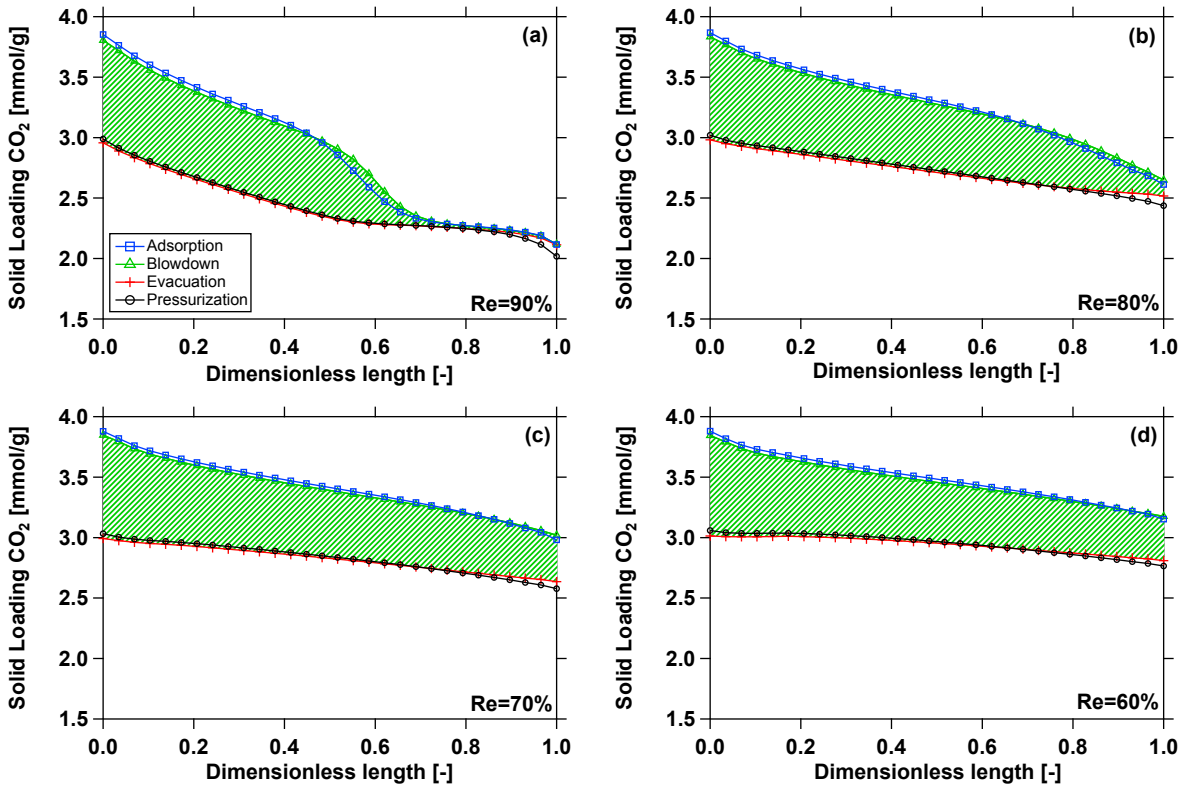


Figure 3.3: Solid $CO_2$ phase profiles in Zeolite 13X is presented for each stage of the 4-step PSA cycle with 95% purity and varying recoveries: (a) $Re_{CO_2}$=90%, (b) $Re_{CO_2}$=80%, (c) $Re_{CO_2}$=70% and (d) $Re_{CO_2}$=60%. The shaded region in each plot represents the amount of $CO_2$ extracted during the evacuation step.

of natural gas, while the latter is a common composition found in exhaust streams from the cement industry and a good composition to analyze the effects of reduced recovery for a feed richer in $CO_2$. In this case study, the performance using zeolite 13X is considered.

Fig. 3.4 shows the minimum energy and maximum productivity at different recoveries for the three feed compositions mentioned previously. At a feed concentration of 8%, with the current cycle and range of decision variables, it is not possible to achieve a $Re_{CO_2}$>90% while reaching a $Pu_{CO_2}\geqslant$95%. As expected, higher $CO_2$ concentrations naturally result in lower energy consumption and higher productivity. It can be seen that the rate of change of energy and productivity with respect to recovery is more pronounced for $y_{CO_2}$=0.20 compared to $y_{CO_2}$=0.08. Figs. 3.4 (c) and (d) show the trends of decision variable as a function of the recovery. For the case of minimizing energy, there is a clear difference between the cases of $y_{CO_2}$=0.20 and $y_{CO_2}$=0.08, with the latter naturally requiring lower values of $P_{\text{low}}$. A similar trend is observed for $P_{\text{int}}$. For the case of maximizing productivity, the optimizer chose to operate $P_{\text{low}}$ at the lowest allowable pressure, irrespective of the feed composition. However, the value of $P_{\text{int}}$ were dependent on the

feed composition. A lower feed composition required lower values of $P_{\text{int}}$. Finally, Figs. 3.4 (e) and (f) show the energy-productivity Pareto curves for different values of recovery. The impact of recovery is more pronounced in the case of $y_{CO_2}$=0.20 compared to $y_{CO_2}$=0.08. For instance, at an energy consumption of 189 $kWh_e/tonne_{CO_2}$, a 51% productivity increase can be achieved by reducing the recovery from 80% to 70% for $y_{CO_2}$=0.08. By reducing the recovery from 90% to 80% at 120 $kWh_e/tonne_{CO_2}$, productivity can be improved by 80% in the case of $y_{CO_2}$=0.20.

### 3.3.3 Impact of the solid adsorbent

In the previous sections, the ability to improve the process performance by reducing the recovery constraint was demonstrated. In this section, the impact of the recovery requirement for various adsorbents is explored. For this purpose, three additional materials are chosen, namely CS-AC, UTSA-16 and the hypothetical Lowest Energy Isotherm Material. They will be analyzed following the same methodology presented in the previous chapters for Zeolite 13X. The physical properties of these materials and the isotherm parameters are presented in Table 3.1 and 3.2. For each adsorbent, the three optimizations were carried out (i.e. energy-recovery, productivity-recovery and energy-productivity). Identical column dimensions, cycle configuration, decision variables and upper and lower bounds were used. The results of this study are presented in Fig. 3.5.

Fig. 3.5 (a) shows the results of the maximization of recovery and minimization of energy consumption. Overall, the materials showed similar trends as seen for Zeolite 13X, where the impact of recovery constraint was more pronounced at the high recovery end. CS-AC presented the highest energy consumption for the values of recovery analyzed and could not achieve $Re_{CO_2}$=90% under the considered range of the decision variables. On the other hand, UTSA-16 performed better than Zeolite 13X at any recovery value, attaining values close to the Lowest Energy Material. The corresponding $P_{\text{low}}$, $P_{\text{int}}$ and bed utilization for UTSA-16 can be seen in Fig. 3.5 (b). If compared to Zeolite 13X for the same recovery values, it can operate at higher pressures and presents a higher bed utilization, which translates into lower energy consumption. It is also worth noting that when using UTSA-16 (with $Pu_{CO_2}$>95% and $Re_{CO_2}$≈40%), it is possible to achieve a low energy operation at $P_{\text{low}}$ of 0.1 atm. This is an important result which demonstrates that the requirement of low vacuum pressures can be avoided by operating at lower recoveries.

The productivity-recovery Pareto curves for all solid adsorbents and the corresponding decision variables for UTSA-16 can be seen in Fig. 3.5 (c) and (d) respectively. Looking at the first figure, we can see that all materials present a similar trend as seen for Zeolite 13X, where large improvements are obtained at first when reducing recovery, followed by a more moderate gain. The Pareto curve for UTSA-16 presents the highest productivity and the highest productivity

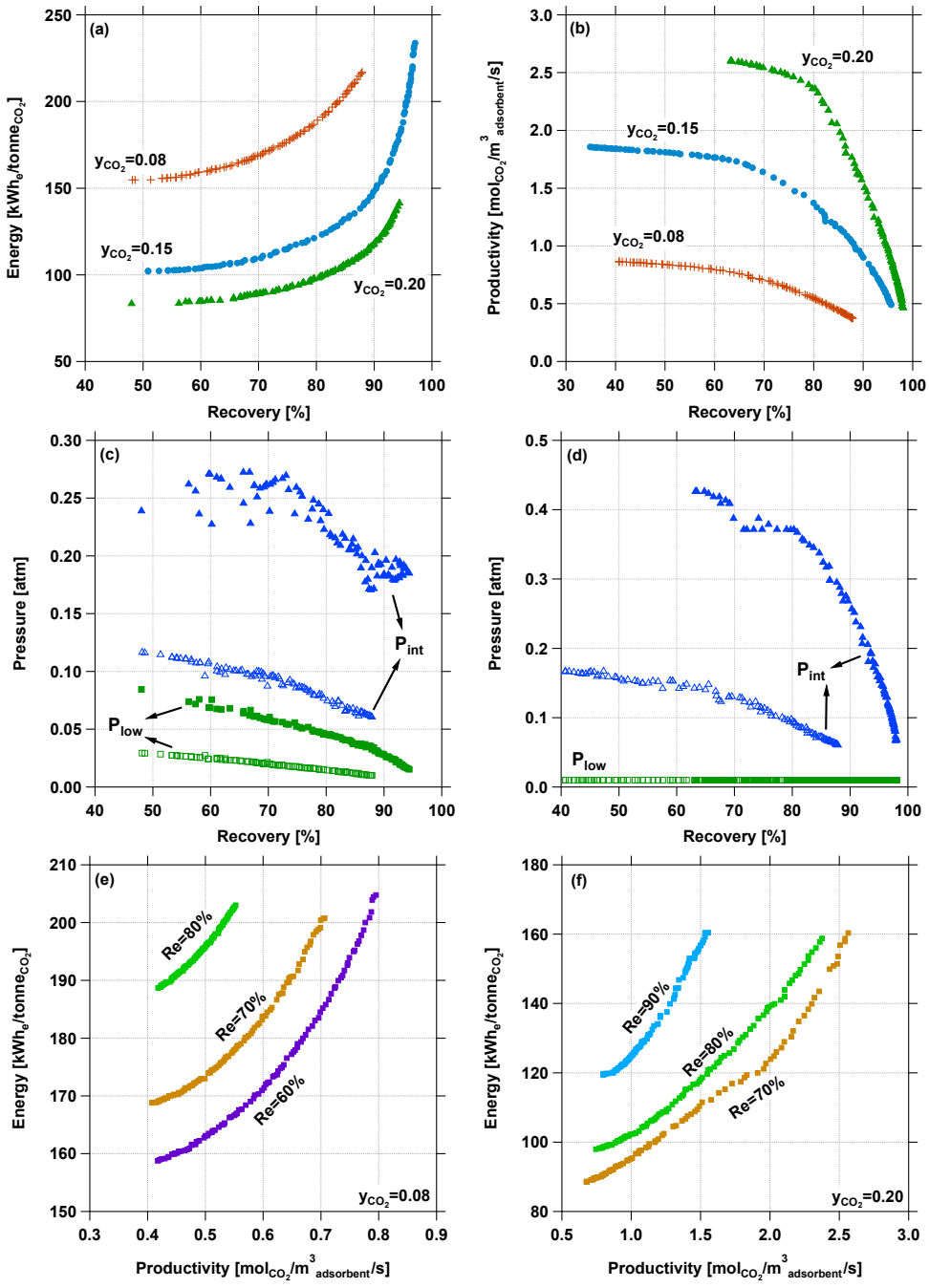


Figure 3.4: Impact of flue gas compositions on (a) Energy-recovery and (b) productivity-recovery Pareto curves. (c) and (d) are comparisons between decision variables corresponding to the Pareto curves shown in sub-figures (a) and (b), respectively. The opened symbols represent the operating pressures for $y_{CO_2}$=0.08 and the closed symbols for $y_{CO_2}$=0.20. The energy-productivity Pareto curves for fixed $CO_2$ recovery values are also presented considering (e) $y_{CO_2}$=0.08 and (f) $y_{CO_2}$=0.20.

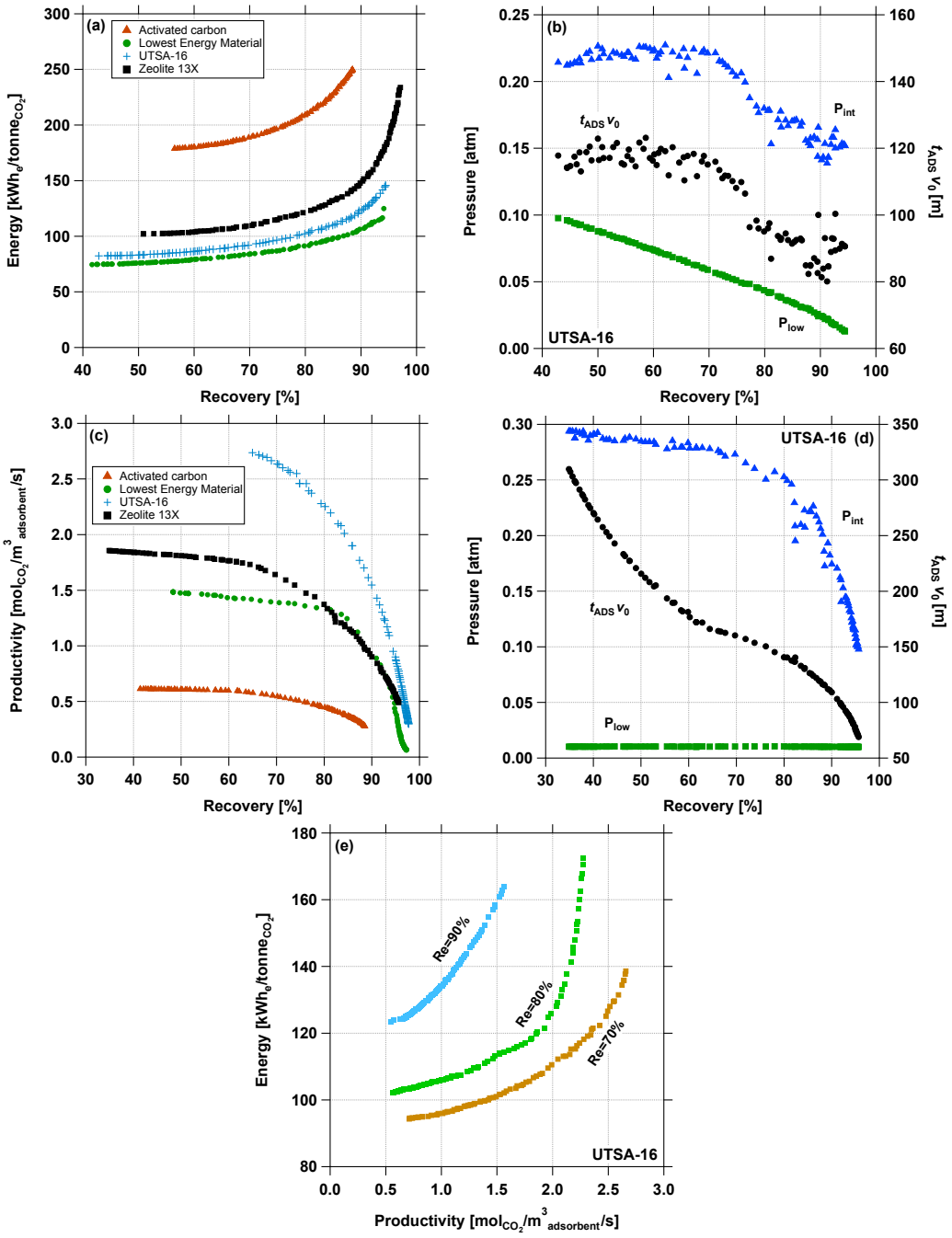


Figure 3.5: Impact of recovery for different adsorbents. (a) Comparison of energy-recovery Pareto curves for four different adsorbents. (b) Trends for decision variables corresponding to the Pareto curve of UTSA-16 shown in sub-figure (a). (c) Comparison of productivity-recovery Pareto curves for different adsorbents. (d) Trends for decision variables corresponding to the Pareto curve of UTSA-16 shown in sub-figure (c). (e) Comparison of energy-productivity Pareto curves for UTSA-16 at fixed $CO_2$ recovery values.

increase rate as recovery decreases. An interesting observation is the difference between the Pareto curves of UTSA-16 and Zeolite 13X. At high recovery requirements, the first material performs marginally better than the latter. However, at lower recovery values, the advantage of UTSA-16 is significantly enhanced. Considering the allowed range of the decision variables, the Pareto curve for UTSA-16 could not achieve $Re \leqslant 60\%$ since it hit the highest feed velocity allowed of 2.5 m/s. It also presented a much higher bed utilization when compared to the previously presented Zeolite 13X, which leads to the increase in productivity. The solid phase profiles for UTSA-16 are shown in the Supporting Information. Similar observations as in Fig.3.3 can be made for UTSA-16.

The relation between minimum energy and maximum productivity for UTSA-16 can be analyzed in Fig. 3.5 (e) at three different $CO_2$ recoveries. For the energy consumption of 120 $kWh_e/tonne_{CO_2}$, the productivity can be improved by approximately 500% by lowering the recovery from 90% to 70%. This is a remarkable improvement.

### 3.3.4 Impact of vacuum pump efficiency

Thus far, the energy calculations have been considering that both the compression and evacuation pumps operate with fixed values of efficiency ($\eta$), independently of the operating conditions. In a real case scenario though, vacuum pump performance tends to be highly dependent on the pressures at which they are operating. To put that into perspective, after analyzing a group of pump curves, we noticed that efficiency tends to be constant at moderate vacuum (e.g. $P_{\text{low}}$>0.1) bar and starts to drop sharply at lower pressures. In order to account for variations in the efficiency as a function of operation pressures, an empirical equation was used:

$$\eta = 0.8 \frac{19.75\, P}{1 + 19.75\, P} \tag{3.9}$$

where $P$ is the pressure given in bar. Note that this is not a rigorous expression, but one that describes the overall trend found in the literature. The goal here was to see how the performance of the VSA process would change as we consider a more realistic description of the vacuum pump efficiency. We were interested in verifying if this would discourage the optimizer to move towards low values of $P_{\text{low}}$.

Fig. 3.6 (a) shows the same energy-productivity Pareto curves seen in Fig. 3.2 (f), but this time calculated with varying $\eta$. By comparison, the new curves show a much higher energy consumption, being as much as four times higher in high productivity scenarios. This drastic increase can be explained by analyzing the new values of efficiency achieved throughout the VSA process, where at $P_{\text{low}}$=0.01 atm for example, it is as low as $\eta$=13.8%. Considering that the evacuation step is the main contributor to the overall energy consumption in the system,

a decrease in $\eta$ in this step is very impactful and explains the difference seen. However, by analyzing the decision variables from the Pareto curve with varying $\eta$ presented in Fig. 3.6 (b), we can see that not only their trend, but also the overall values are very similar when compared with the fixed $\eta$ scenario. Even though the overall values of energy consumption drastically differ with this new approach to pump efficiency, the values of productivity, the optimal operating conditions and overall trend of the energy-productivity Pareto curves are maintained, therefore, showing that the same conclusions obtained in the previous section for fixed $\eta$ regarding reduced $CO_2$ recoveries can be applied here as well.

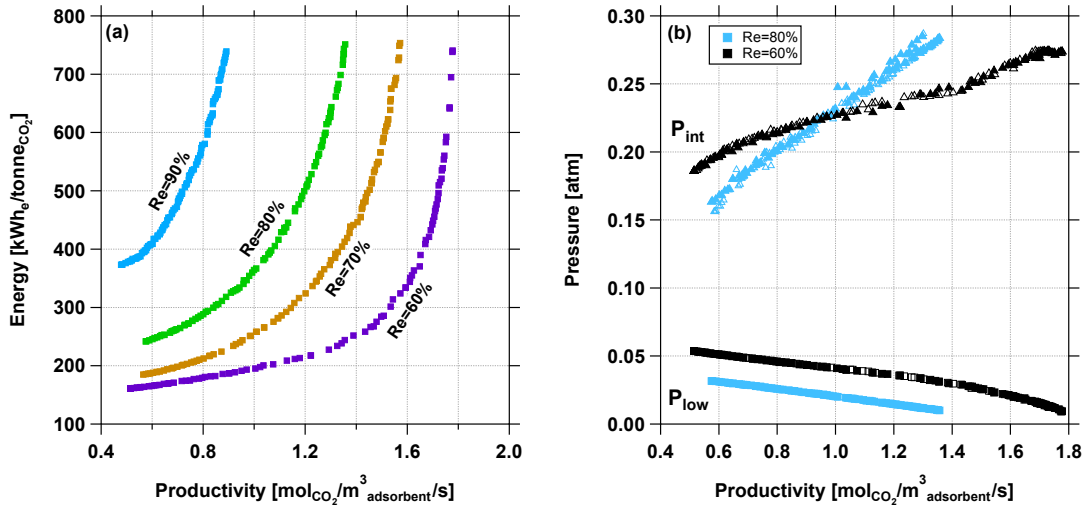


Figure 3.6: (a) Energy-productivity Pareto curves at different $CO_2$ recovery values considering a varying vacuum pump efficiency. (b) Comparison between the operating pressures of the energy-productivity Pareto curves shown in sub-figure (a) for $Re_{CO_2}$=80% and $Re_{CO_2}$=60%, with fixed (represented by open symbols) and varying (closed symbols) pump efficiency.

## 3.4 Conclusions and perspectives

This paper studied the effect of reduced recovery on a 4-step VSA process for post-combustion $CO_2$ capture. The detailed analysis was carried out based on the Pareto fronts obtained from rigorous process optimization employing a detailed computational model. The one dimensional, non-isothermal, non-isobaric process simulator was coupled with a genetic algorithm to perform three multi-objective optimizations, namely, energy-recovery, productivity-recovery and energy-productivity, subject to the constraint of 95% $CO_2$ purity. A 4-step VSA process with zeolite 13X as adsorbent was considered as the base case for performing all three multi-objective optimizations. It was found that lowering the recovery targets significantly impacts the energy consumption and productivity of the VSA process, where a reduction of $CO_2$ recovery from 90% to 70% resulted in a 26.7% energy consumption drop and a 82.3% productivity increase.

The lowered recovery targets enabled higher operating pressures and bed utilization. Further, different case studies were analyzed to understand the impact of reduced recovery on the type of adsorbent, feed composition and pump efficiency. In the first case study, multiple adsorbents were selected and their performance under reduced recovery constraints analyzed. It was found that even by changing the adsorbent, the improvements in the process performance are significant and follow a similar trend as seen for zeolite 13X. A second case study was carried by performing parametric analysis on the feed composition under reduced recovery targets. For all feed compositions, the energy consumption of the process reduced and productivity increased with lower recoveries, with streams richer in $CO_2$ presenting a higher rate of improvement. Finally, in order to model the energy consumption closer to realistic conditions, the pressure dependence of the vacuum pump efficiency was taken into account. The resulting Pareto curves showed a significant increase in energy consumption, however, it kept the overall trend, the productivity values and the operating conditions as seen for the fixed efficiency case.

This paper demonstrates how reducing the recovery constraint can lead to significant improvements in energy consumption and productivity. The following aspects provide additional perspectives as to why this approach should be pursued:

1. The few papers that deal with VSA-based post-combustion capture indicate practical limitations on vacuum pump capacities, maximum column sizes and the necessity of several hundred trains (with multiple columns each) in order to capture 90% of $CO_2$ that is emitted from a coal-based power plant. These results raise genuine questions about the complexity involved in scale-up. Reduced recovery designs, such as the one presented in this paper, could alleviate some of the concerns. The study on the impact for different flue gas compositions indicate that the reduced recovery is more effective when $CO_2$ composition is high. This might be very favorable for situations such as $CO_2$ capture in cement plants, where the concentration of $CO_2$ in the flue gas is high and the flow rates are lower compared to coal-based power plants.

2. The issue of multiple trains has another impact on the costs. On one hand, processes such as absorption can be scaled-up to handle much larger gas throughput, they benefit from economy of scale. The well-known $6/10^{\text{th}}$ rule will reduce the costs as the plant size grows. On the other hand, since the scale-up of VSA units is achieved by multiplexing, economy of scale cannot be achieved. In other words, reducing the recovery through venting a portion of the flue gas is unlikely to reduce the costs, therefore, lower recovery constraint in each train is a better option for reducing costs.

3. One of the key bottlenecks in employing VSA processes for $CO_2$ capture is the requirement of low vacuum pressures. Several process optimization studies that have also analyzed the

use of multiple adsorbents and cycles have shown that a low pressure of at least 0.05 bar is required to meet separation targets in a single-stage. Low pressures variably affect vacuum pump efficiency, which can increase the parasitic energy consumption. Naturally, this limitation can be overcome by operating in two-stages. However, this arrangement can reduce the overall productivity, which would impact the costs. As shown in this study, lowering recovery targets allow operations at pressures of $\approx 0.1$ bar, which makes practical implementations more attractive.

4. Finally, as observed in the NETL report, reduced recovery capture increases the opportunities to scale-up VSA processes and increase the experience in order to advance this technology.

This paper also provides the motivation to study low recovery options and possibly develop costing methodologies to explore and compare capture alternatives. Future work will focus on how the indicators of productivity and energy translate into the cost of capture and possible experimental demonstrations.

# Chapter 4

# Modeling, simulation and validation of an adsorption-based pilot-scale pre-combustion $CO_2$ capture unit

## 4.1 Introduction

In recent years, drastic increases of carbon dioxide concentrations have been observed in the atmosphere, clearly due to anthropogenic causes [28]. As a result of these environmental concerns, government bodies, the scientific community and business enterprises have been adopting actions to reduce the emission of greenhouse gases and the overall anthropogenic impact on the environment, including the reduction of $CO_2$ emissions in the energy sector. Pre-combustion $CO_2$ capture in Integrated Gasification Combined Cycle (IGCC) power plants is an option to fulfill the human necessities for energy consumption, while avoiding endangering the environment with the emission of harmful gases. IGCC power plants are characterized by the production of synthesis gas (i.e. syngas) from coal (or other fossil fuel material) through gasification, a process in which the carbonaceous material is converted at high pressures and temperatures in the presence of steam and a catalyst. The product of gasification reactors is mainly composed of $H_2$, CO and $CO_2$. The gas mixture is then sent to Water-Gas Shift (WGS) reactors, where the CO is further converted in the presence of steam into more $CO_2$ and $H_2$. The $CO_2$ can then be captured and the resulting pure $H_2$ used as fuel, producing energy while emitting only water vapor. An schematic of IGCC power plants with $CO_2$ capture can be seen in Fig. 4.1.

TDA Research Incorporated had recently installed and operated an adsorption-based $CO_2$ capture unit in Wilsonville, Alabama, USA. The PSA unit was integrated to the National Carbon Capture Center (NCCC), from which it received the syngas to be treated. The separation facility

had the objective of testing different operation schemes, analyzing the long-term performance of the system and demonstrate the techno-economic viability of this technology [51]. The facility used a new adsorbent developed by TDA Research Inc. It is a mesoporous activated carbon (i.e. pores will not limit diffusion, while presenting high surface areas) which presented strong $CO_2$ affinity through physical adsorption. The bonds are robust enough to allow the PSA to be operated at high temperatures, with regeneration energies being comparable to state-of-art absorbents [51].

The main goal of this chapter is to model TDA's $CO_2$ capture unit and validate it by comparing with the data collected during day-to-day operations. By detailed process modeling, the complex PSA unit installed in Alabama can be computationally simulated with a set of constitutive equations and boundary conditions. *In silico* experiments can support the separation unit on the field. A reliable model can be used to test new cycles and optimize the process operations faster and at lower costs.

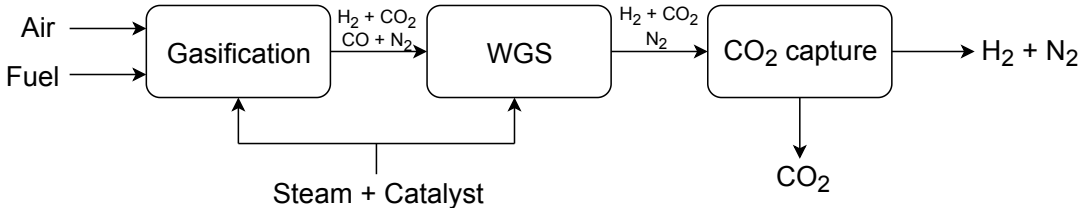


Figure 4.1: Schematic of an IGCC power plant with an air-blown gasifier and $CO_2$ capture.

### 4.1.1 Pilot-scale adsorbent-based $CO_2$ capture unit

The synthesis gas stream to be cleaned is provided by NCCC. The gasification operates through air blown glasifiers, therefore, it will contain a substantial amount of $N_2$. A schematic of the pilot scale facility operated by TDA Research Inc. can be seen in Fig. 4.2. It is composed of different equipment working in parallel in order to capture $CO_2$ and purify $H_2$. Moreover, it can be divided into three main parts. The first stage includes the desulfurization column and the trace contaminant removal beds. This step is important in order to clean the syngas received from NCCC from sulfur based molecules (e.g. $H_2S$), trace metals, heavy organic compounds and other contaminants. These molecules are extremely harmful to the environment and cannot be emitted to the atmosphere. If not removed, they could also decrease the $CO_2$ capture efficiency in the adsorption steps and reduce the chemical stability of the adsorbent and its operating lifetime. The unit also includes its own steam generator, responsible to supply the superheated steam necessary for the WGS reaction and to regenerate the adsorption columns.

The second step of the pilot plant is the WGS reaction, which has the objective of converting CO and $H_2O$ into $CO_2$ and $H_2$ in the presence of a catalyst. This step is essential to increase the

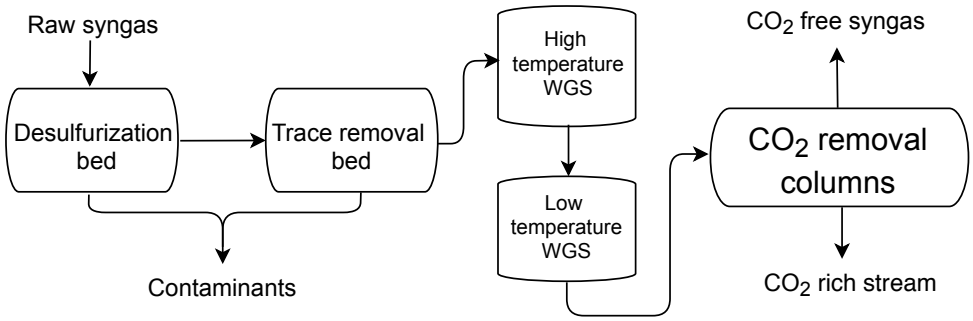


Figure 4.2: Schematic of TDA's pilot plant unit.

overall $H_2$ conversion, hence, the power plant's productivity. TDA Research operated three WGS reactors at different operating conditions. The first WGS reactor operates at high temperatures and with an iron-based catalyst. The second WGS reactor presents similar operating conditions as the previous one and can be bypassed depending on the remaining CO and steam content present in the product line. The last WGS reactor operates at lower temperatures and with a cooper-based catalyst. At the end, the combination of all WGS reactors resulted in CO conversions above 96%. Water knock-out tanks were also installed in different stages of the process in order to capture the condensed water vapor.

The third stage is the $CO_2$ capture unit is composed of eight adsorption columns operating in parallel, filled with an adsorbent synthesized in-house by TDA, henceforth referred to as TDA 2017. The columns were insulated and heat exchangers were installed around each of them in order to better control the heat effects in the equipment. The PSA cycle adopted can be seen in Fig. 4.3. It is composed of eleven steps:

- High pressure adsorption (ADS) to trap $CO_2$ and produce clean syngas;
- 3 pressure equalization donor steps (EQD1, EQD2, EQD3) to lower the pressures and maximize $H_2$ recovery;
- Co-current blowdown (Co-BD) to extract the light product;
- Counter-current blowdown (Cn-BD) to extract the heavy product;
- Counter-current purge (PU) with superheated steam to extract $CO_2$ and regenerate the column;
- 3 pressure equalization receiver steps (EQR1, EQR2, EQR3);
- Product pressurization (PRESS).

Depending on the cycle schedule, operating valves control the flow of syngas, directing it to

one of the columns. All lines are monitored and heated in order to avoid the condensation of water or any other component (i.e. assure that they will be above the dew point temperature). Gas flow meters and gas flow controllers were installed to measure and control the syngas flow rate, pressure transducers to measure the operating pressures and pressure drop and eleven gas samples were taken at different points in the process to constantly monitor the fluid phase compositions.

Since this thesis has the objective of modeling the PSA unit, it will be restricted to studying and simulating only the third section of the pilot plant.

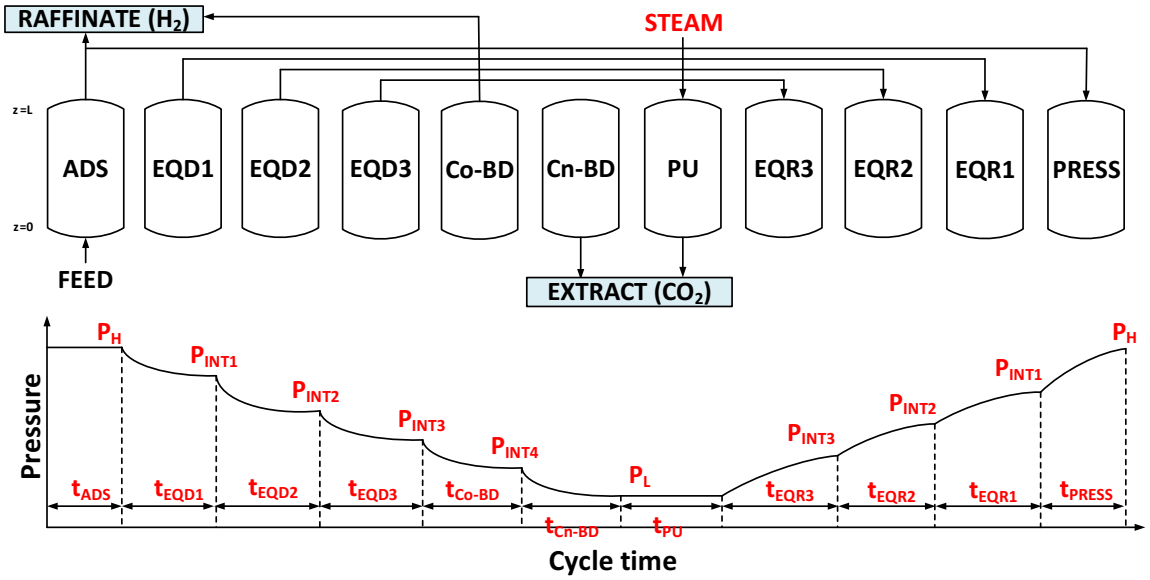


Figure 4.3: 11-step PSA cycle operated at the IGCC power plant to capture $CO_2$.

## 4.2 Modeling and simulation

To model the 11-step PSA for pre-combustion $CO_2$ capture, a system of partial differential equations is considered. The detailed constitutive equations and the boundary conditions can be found in Appendix A. With them, total mass balance, component mass balances, energy balance and momentum balance equations are solved with a finite volume method and a built-in MATLAB ODE solver function. The simulations run for a minimum of 35 cycles and until the mass balance errors were smaller than 1%, from where it was considered that the system reached cyclic steady state condition. Pre-combustion and post-combustion $CO_2$ capture through PSA present intrinsic similarities, therefore, both systems can be similarly modeled. More details about it, including the modeling assumptions, can be found in Chapter 3.

Product purity and recovery are performance indicators and commonly used as process con-

straints. It is worth mentioning that purity can be defined in two ways: wet purity and dry purity, where the difference between them is the presence of water content in the calculations. In this chapter, we will be working with wet purity. The performance indicators are defined as:

$$Pu_{\mathrm{CO_2}}[\%] = \frac{n_{\mathrm{CO_2}}^{\mathrm{Cn-BD}} + n_{\mathrm{CO_2}}^{\mathrm{PU,out}}}{n_{\mathrm{total}}^{\mathrm{Cn-BD}} + n_{\mathrm{total}}^{\mathrm{PU,out}}} \times 100 \tag{4.1}$$

$$Pu_{\mathrm{H_2}}[\%] = \frac{n_{\mathrm{H_2}}^{\mathrm{ADS,out}} - n_{\mathrm{H_2}}^{\mathrm{PRESS,in}} + n_{\mathrm{H_2}}^{\mathrm{Co-BD}}}{n_{\mathrm{total}}^{\mathrm{ADS,out}} + n_{\mathrm{total}}^{\mathrm{Co-BD}}} \times 100 \tag{4.2}$$

$$Re_{\mathrm{CO_2}}[\%] = \frac{n_{\mathrm{CO_2}}^{\mathrm{Cn-BD}} + n_{\mathrm{CO_2}}^{\mathrm{PU,out}}}{n_{\mathrm{CO_2}}^{\mathrm{feed}}} \times 100 \tag{4.3}$$

$$Re_{\mathrm{H_2}}[\%] = \frac{n_{\mathrm{H_2}}^{\mathrm{ADS,out}} - n_{\mathrm{H_2}}^{\mathrm{PRESS,in}} + n_{\mathrm{H_2}}^{\mathrm{Co-BD}}}{n_{\mathrm{H_2}}^{\mathrm{feed}}} \times 100 \tag{4.4}$$

In order to model the adsorption equilibrium effects in the columns, single component Sip's isotherm was chosen:

$$q_i{}^{*} = \frac{q_{s,i}(k_i P_i)^{s_i}}{1 + (k_i P_i)^{s_i}} \tag{4.5}$$

$$q_{s,i} = \omega_i \; e^{-\psi_i / RT} \tag{4.6}$$

$$k_{_i} = \theta_i \; e^{-\phi_i / RT} \tag{4.7}$$

$$s_i = s_{1,i} \; atan\big[s_{1,i}(T - T_{\mathrm{ref}})\big] + s_{\mathrm{ref},i} \tag{4.8}$$

where $q_{\mathrm{s,i}}$ is the solid saturation loading, $k_{\mathrm{i}}$ is the adsorption equilibrium constant and $s_{\mathrm{i}}$ describes the homogeneity of the adsorbent's surface, varying from 0 to 1. This equilibrium model is a modification of the Freundlich Isotherm model, however, it also accounts for the adsorbent saturation at high pressures. Sip's isotherm has been successfully used in previous studies to model the equilibrium data of pre-combustion $CO_2$ capture using TDA AMS-19 [52,53], a similar activated carbon as the one presented in this chapter.

## 4.3 Simulation parameters and measured data

The simulation of the pilot-scale adsorption unit requires the acquisition of plenty of different parameters, where they could be measurements from the day-to-day on-site operations, measured in previous in-house experiments, found in literature or fitted/assumed. This section focuses on the acquisition of these parameters.

| | | |
|---|---|---|
| Bed length, $L$ [m] | 2.36 | measured |
| Column inner radius, $r_{\text{in}}$ [cm] | 165.0 | measured |
| Column outer radius, $r_{\text{out}}$ [cm] | 168.0 | measured |
| Bed voidage, $\varepsilon$ [-] | 0.2505 | measured |
| Particle voidage, $\varepsilon_{\text{p}}$ [-] | 0.368 | assumed |
| Particle radius, $r_{\text{p}}$ [mm] | 0.30 | assumed |
| Tortuosity factor, $\tau$ [-] | 3.0 | assumed |
| Density of the solid particle, $\rho_{\text{p}}$ [kg/m$^3$] | 830.5 | assumed |
| Density of the column wall, $\rho_{\text{s}}$ [kg/m$^3$] | 7,800 | standard |
| Effective heat conduction coefficient, $K_z$ [J/m/s/K] | 0.0903 | assumed |
| Thermal conductivity of the wall, $K_{\text{w}}$ [W/m/K] | 16.0 | standard |
| Inside heat transfer coefficient, $h_{\text{in}}$ [W/m$^2$/K] | 25.0 | assumed |
| Outer heat transfer coefficient, $h_{\text{out}}$ [W/m$^2$/K] | 500.0 | assumed |
| Gas specific heat capacity, $C_{p,\text{g}}$ [J/kg/K] | 1,010.6 | standard |
| Adsorbent specific heat capacity, $C_{p,\text{s}}$ [J/kg/K] | 1,100 | assumed |
| Wall specific heat capacity, $C_{p,\text{w}}$ [J/kg/K] | 502.0 | standard |
| Adsorbed phase specific heat capacity, $C_{p,\text{a}}$ [J/kg/K] | 1,010.6 | assumed |
| Fluid viscosity, $\mu$ [kg/m/s] | $2.15\times10^{-5}$ | assumed |
| Molecular diffusivity, $D_m$ [m$^2$/s] | $4.81\times10^{-8}$ | assumed |
| Adiabatic constant, $\gamma$ [-] | 1.4 | assumed |
| Ambient temperature, $T_{\text{a}}$ [K] | 493.15 | assumed |
| Feed temperature, $T_{\text{f}}$ [K] | 452.15 | measured |
| Purge temperature, $T_{\text{f}}$ [K] | 406.15 | measured |
| Feed velocity, $T_{\text{f}}$ [m/s] | 0.103 | measured |
| Purge velocity, $T_{\text{f}}$ [m/s] | 0.262 | measured |
| Universal gas constant, $R$ [m$^3$Pa/mol/K] | 8.314 | standard |

Table 4.1: Modeling parameters for the pre-combustion $CO_2$ capture pilot unit.

### 4.3.1 Solid sorbent

The adsorbent (TDA 2017) is a mesoporous activated carbon material with high selectivity for $CO_2$ and with the possibility of operating at high temperatures (i.e. above the dew point of the gas mixture). The isotherm properties of the material can be seen in Table 4.2. The adsorption equilibrium data of $CO_2$ for TDA 2017 was assumed to be the same as the one measured for TDA 2015 (a material also synthesized by TDA that presented similar characteristics [54]), while water was considered non-adsorbent. However, for the equilibrium data of $H_2$ and $N_2$, the values had to be assumed based on the literature. They were based on previous studies with a similar activated carbon [52, 55]. Other adsorbent characteristics including particle diameter, internal porosity, heat of adsorption, density and specific heat capacity were assumed to be the same as for TDA 2015, which were measured in previous studies [54]. Tortuosity was considered to be 3, a common value reported in the literature [1].

| | $\omega_i$ [mol/kg] | $\psi_i$ [kJ/mol] | $\theta_i$ [1/Pa] | $\phi_i$ [kJ/mol] | $s_{1,i}$ [-] | $s_{2,i}$ [-] | $s_{\text{ref}}$ [-] | $T_{\text{ref}}$ [K] |
|---|---|---|---|---|---|---|---|---|
| $CO_2$ | 3.31 | -11,757 | $1.189\times10^{-9}$ | -5.09 | $4.07\times10^{-2}$ | $2.64\times10^{-3}$ | 0.7602 | 281.0 |
| $H_2/N_2$ | 6.66 | 0.0 | $0.7\times10^{-9}$ | -9.83 | 0.0 | 0.0 | 0.956 | 273.0 |

Table 4.2: Single component Sip's isotherm parameters.

### 4.3.2 Adsorption column

The adsorption columns were designed by TDA Research Inc., based on the performance of previous lab and pilot scale experiments and computational modeling of the PSA process. The dimensions of the columns (column height, internal and external diameters, etc.) were obtained through the detailed mechanical drawings of the equipment, while bed voidage was measured by TDA. Bulk density and mass of adsorbent could then be calculated. Other physical properties including internal heat transfer coefficient, effective heat conduction coefficient and heat capacity of the gas phase were based on previous PSA studies [1, 54]. The column walls were built with stainless steel, hence, properties like wall density, heat capacity and thermal conductivity were standard values found in literature. Fluid viscosity and molecular diffusion were taken from standard values for $N_2/CO_2$ mixtures [52].

As previously mentioned, heat exchanger insulated jackets were installed around each adsorption column in order to control the operating temperatures. To simulate the effect of intense heat being transfered through the column's walls, the external heat transfer coefficient was assumed to be 500 $J/m^2/s/K$. This extremely high value is expected to be high enough to create instantaneous heat transfer from the wall to the environment. In this case, the ambient temperature is used to represent the jacket's temperature, which was measured with thermocouples at the walls.

### 4.3.3 Operating conditions

Throughout its operating life in Alabama, the pilot unit tested not only the techno-economic feasibility of PSA for $CO_2$ capture in IGCC power plants, but it also tested different operating conditions. In this subsection, the operating conditions required as input for the computational model are obtained by analyzing the day-to-day on-field measurements from the pilot unit.

The time required in each step were based on experimental set points, hence, it does not vary when at cyclic steady state. They are provided in Table 4.3. It is worth mentioning that the idle times in between cycles were also included in the simulations, however, they are not in the table. The feed and purge stream properties (i.e. volumetric flow rate, temperature and pressure) were measured at the beginning of the PSA skid (before the lines were diverted into a single column) and after the adsorption columns in both heavy and light product lines. The molar compositions of the streams are shown in Table 4.4. With this data, stream velocities and molar flow rates can be calculated.

| $t_{ADS}$ [s] | $t_{EQ1}$ [s] | $t_{EQ2}$ [s] | $t_{EQ3}$ [s] | $t_{Co-BD}$ [s] | $t_{Cn-BD}$ [s] | $t_{PU}$ [s] | $t_{PRESS}$ [s] |
|---|---|---|---|---|---|---|---|
| 120 | 30 | 30 | 30 | 30 | 60 | 120 | 30 |

Table 4.3: Cycle times for the 11-step PSA process.

The adsorption columns were designed to be completely instrumented in both radial and axial directions. In total, 15 thermocouples were installed in each bed, providing measurements at 4 different lengths and 3 different diameters. The thermocouples closest to the walls were assumed to be the ambient temperature (i.e. the heat exchanger insulated jacket's temperature), while the measurements at each length were averaged out. This assumption is necessary when comparing the on-field collected data and the computational results, since the latter is based on a 1-D model without radial dispersion.

It is important to mention that some precautions were taken in order to standardize the estimation of the operating conditions previously mentioned, since the unit operated for more than 20 days. Initially, all the collected data was analyzed considering the stability of the temperature, pressure, concentration and flow rate measurements. Days with measurement spikes or measurement stoppages were not considered. The operating conditions and overall process and cycle stability were considered as well, hence, days with bypass lines or with gas flaring were discarded. In the end, it was analyzed if the PSA unit operated at cyclic steady state throughout the whole day of operations. Considering all the aforementioned requisites, a single day of operation was chosen and the operating conditions taken as an average of that data. The performance indicators (e.g. purity and recovery) in the next section are obtained following the same methodology.

| | $y_{CO_2}$ [%] | $y_{H_2}$[%] | $y_{H_2O}$[%] | $y_{N_2}$[%] |
|---|---|---|---|---|
| Feed | 16.4 | 12.3 | 8.1 | 63.2 |
| Purge | 0.0 | 0.0 | 100.0 | 0.0 |

Table 4.4: Feed and purge stream compositions.

## 4.4 Results and discussion

Light and heavy products purity and recovery are important performance indicators and will be analyzed first. Considering the flow rates and compositions collected on a single day of operations (i.e. April 10th, 2017) under cyclic steady state conditions, the average purity and recovery values for that day are presented in Table 4.5. The computationally simulated results are also included for comparison.

| | $Pu_{CO_2}$[%] | $Pu_{H_2}$[%] | $Re_{CO_2}$[%] |
|---|---|---|---|
| Experimental | 20.4 | 13.9 | 94.0 |
| Simulated | 34.1 | 18.4 | 100.0 |

Table 4.5: Light and heavy products purity and recovery for both field measurements and simulated results.

The simulated data obtained from the model shows higher purity and recovery, for both $CO_2$ and $H_2$. It is interesting to notice that the simulations show $Re_{CO_2} = 100.0\%$, which is an indication that the bed is only being partly utilized. It goes against the results obtained on the field, which presents a lower recovery value, hence, the presence of $CO_2$ in the light product. In order to analyze and fully understand the discrepancy between simulated and experimental results, temperature, pressure and concentration profiles inside the columns were analyzed as well.

Fig. 4.4 shows the pressure and temperature profiles in the adsorption column throughout one complete cycle, where the solid lines represent the simulated results and the dashed lines represent the data acquired on the field. It is worth mentioning that the pressure and temperature experimental data presented here are not average values, but the data collected in one of the cycles performed. Since the system is at cyclic steady state condition, it was assumed that it could be used as a good representation of the overall physics in the columns. The pressure profiles are shown in Fig. 4.4 (a), where it is possible to notice a close match between results. The simulated profile was able to represent the transient pressure in the column, matching not only the overall operating pressures but also the evacuation and pressurization transitions. On the other hand, the temperature profiles at different lengths in the column are presented in Fig. 4.4 (b), (c) and

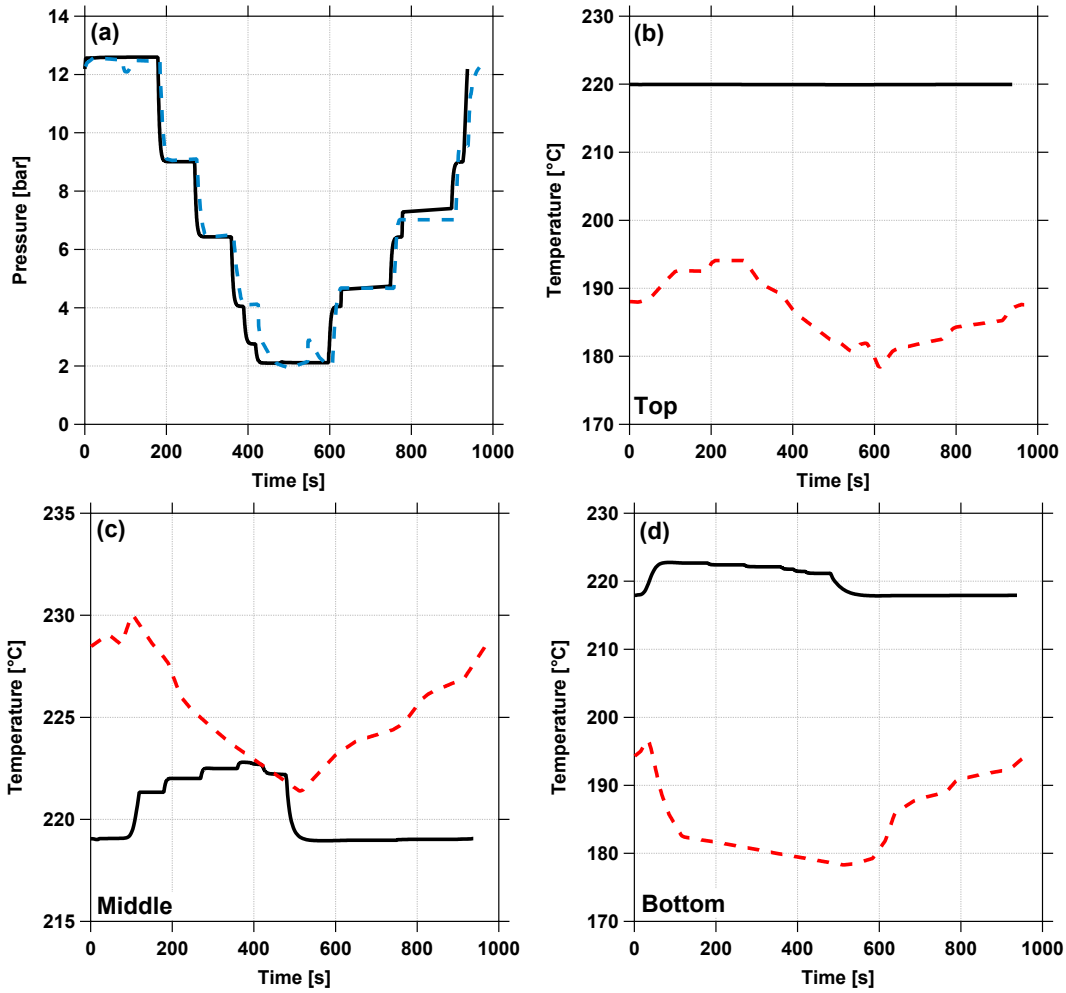


Figure 4.4: (a) Pressure front at different steps in the PSA cycle. Temperature fronts at the (b) top, (c) middle and (d) bottom of the column. The solid lines represent the results obtained from the simulations, while the dashed lines are the data measured on the site.

(d) and it is possible to notice a discrepancy between experimental and simulated data. The results obtained computationally tend to present less variations, maintaining its temperature close to 220°C, the jacket's temperature. It is interesting to notice that it presented a constant temperature at the top of the column throughout all 11 steps, showing that the temperature front fades as it travels through the bed and that there is little adsorption in that region. The experimental data showed a bigger variation, with regions reaching temperatures below 180°C (due to the feed and purge streams) or as high as 230°C (due to the heat of adsorption). Two main factors should be considered in order to explain the discrepancy seen between results. At first, it is important to analyze the flow rates and $CO_2$ concentration fronts inside the column, since they are going to highly impact the heat fronts. Differently from the simulations, the heat front from the experimental results advances throughout the bed. Secondly, the assumed heat

transfer coefficients could be wrongly impacting the profiles. It is clear that the computational results are being more impacted by the heat exchanger jacket (as seen by the temperature profiles stabilizing at 220°C), while the pilot-plant columns are more impacted by feed and purge stream temperatures and the heat of adsorption (considering that the columns rarely operate at 220°C). For future studies, the heat transfer coefficients could be experimentally measured or fitted through computational optimization. This extra step would ensure that the coefficients are precisely representing the physical phenomenon.

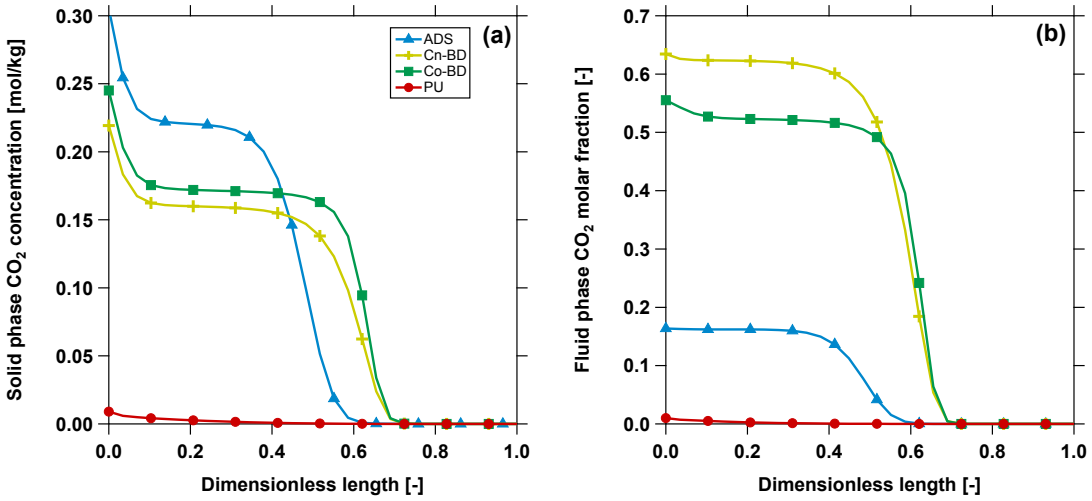


Figure 4.5: Simulated (a) solid and (b) gas phase $CO_2$ fronts at different steps in the PSA cycle.

Fig. 4.5 presents the gas and solid phase $CO_2$ fronts at the end of different steps in the PSA cycle. In the adsorption step, the $CO_2$ front advances only to about 70% of the column. It is noticeable that even in the following steps at lower pressures, it does not advance further, solely increasing its concentration in the first half of the equipment. These profiles clearly show that under these conditions, only a small portion of the bed is being used, explaining the high recovery values achieved from the simulations. It also explains the constant temperature profile seen in Fig. 4.4 (d), since there is no $CO_2$ adsorption at the end of the column, no heat of adsorption is detected either. One explanation for the phenomenon seen previously is that the bed is not being fully regenerated in the pilot-scale unit (Fig. 4.5 (a) shows a complete bed regeneration in the simulations). This would result in the reduction of the working capacity of the bed, enabling the $CO_2$ front to travel further in the simulations, with a possible $CO_2$ breakthrough. Another obstacle could be leaks or flow rate measurement errors in the columns, which would also result in the $CO_2$ front moving further.

## 4.5 Conclusions

This chapter had the objective of computationally modeling and simulating the 11-steps PSA cycle operated by TDA Research Inc., including the adsorption equilibrium of four gases (i.e. $CO_2$, $H_2$, $N_2$ and $H_2O$). The modeling of the adsorption based $CO_2$ capture process required the solution of a system of partial differential equations. Finite volume method and a built-in MATLAB solver were used to satisfactorily solve the PDEs, resulting in mass balance errors lower than 1.0%. The model required the acquisition of different parameters, including data collected in previous in-house experiments, found in literature, fitted/assumed or measurements from the pilot-scale unit. The latter were average values of the data collected in a single day of operations under cyclic steady state condition.

To validate the model and analyze the modeling parameters used, purity and recovery for both light and heavy products were compared at first. The $CO_2$ and $H_2$ purity and $CO_2$ recovery obtained *in silico* are higher than the values measured on the pilot-scale unit. In the simulations, the $CO_2$ does not breakthrough, therefore, $Re_{CO_2} = 100\%$ and the bed is not fully utilized, resulting in the higher values of purity seen as well.

The model also provided an insight on the transient profiles inside the columns. By analyzing the $CO_2$ gas and solid concentration profiles, it can be seen that the $CO_2$ front does not travel far into the column, reaching the furthest during co-current blowdown step. This phenomenon explains the high recovery values obtained and implies that the columns are not being fully utilized, diverging from the actual results obtained from the pilot-plant. The simulated pressure profiles characterized the experimental operating pressures very well, matching the values and transitions presented in every step. On the other hand, temperature profiles presented a significant difference in both absolute values and on the trends throughout the columns.

The heat transfer coefficients for the model were assumed based on previous studies and the design of TDA's PSA columns. Laboratory experiments or computational optimization could be used to fit these coefficients and better represent the thermal effects in the columns. Leaks, poor bed regeneration and flow rate measurement errors could also be impacting the results, since there is a clear difference between how much the $CO_2$ and heat fronts advance through the bed. In the simulations, these fronts reach only approximately 70% of the column, while the experiments showed $CO_2$ and thermal breakthrough. Considering the amount of decision variables present and the complexity of the PSA unit, the model still showed a good representation of the system and can be used for preliminary studies of the unit and the physics inside the columns. The pre-combustion $CO_2$ capture unit has recently been transfered to an IGCC power plant in China, were more tests will be run. The new data can be used in future studies to further enhance the accuracy of the model.

# Chapter 5

# Concluding Remarks

## 5.1 Conclusions

This thesis focused on the modeling, simulation and optimization of three different adsorption-based separation processes: SMB chromatography, pre-combustion and post-combustion $CO_2$ capture through pressure swing adsorption.

Chapter 2 studied the characteristics of BP-SMB chromatography for reduced purity requirements. Explicit equations to calculate productivity were developed based on the local-equilibrium theory for ideal systems with linear isotherms, while computational modeling was used to study non-ideal systems with linear and non-linear isotherms. Grid searches were used to find the operating conditions with highest productivity and lowest energy consumption. The performance indicators from BP-SMB were compared with regular SMB. It was shown that BP-SMB provides not only operational advantages due to its flexibility, but also productivity advantages. The simulations showed that greater productivity is achieved in BP-SMB when the feed is richer in the light component, the Henry constants and selectivity are high and when low extract and raffinate purities are desired.

Chapter 3 focused on the effects of reduced $CO_2$ recovery constraints in post-combustion $CO_2$ capture. PSA units were computationally modeled and multi-objective optimization was used in order to generate Pareto curves with the minimum energy consumption and maximum process productivity at different $CO_2$ recovery targets. Initially, a 4-step VSA cycle with Zeolite 13X as the adsorbent and a feed composition containing 15% $CO_2$ was considered. The effects of partial recovery were also tested for a system with different adsorbents (i.e. UTSA-16, CS-AC and Lowest Isotherm Energy material) and varying feed compositions (i.e. 8% and 20% $CO_2$). The Pareto curves showed clear trade-offs between energy consumption, productivity and $CO_2$ recovery, where big process improvements are obtained when reducing the $CO_2$ recovery target

at first, followed by more moderate changes at the lower recovery end. In the first case study, productivity increased by 82.3% and energy consumption decreased by 26.7% when reducing recovery from 90% to 70%, however, it showed much less significant changes when recovery reduced from 60% to 50%. It was shown that the total amount of $CO_2$ captured and the bed utilization were the two main factors impacting on the trend seen.

Finally, chapter 4 focused on the modeling and simulation of a pre-combustion PSA capture unit. The modeling was based on a separation unit operated by TDA Research Incorporated consisting of eight adsorption columns working together in an eleven step PSA cycle. The column dimensions were obtained from the equipment's mechanical drawings and the adsorbent characteristics were previously measured. Other parameters including feed flowrate and composition, pressure profiles and step times were obtained from measurements on the field. In the end, the column was spatially discretized through a finite volume method and the resulting ODEs were solved with a build-in MATLAB solvers. The simulation results showed that even though some assumptions had to be made, the model was able to simulate the major characteristics of the PSA unit. The $CO_2$ purity and recovery obtained computationally were 34.1% and 100.0% respectively, close to the numbers obtained experimentally: 20.4% and 94.0%. The temperature profiles presented a relatively bigger disparity, which could be associated with the assumptions made during modeling or measurement errors and leaks in the PSA unit. Even though there are some discrepancies between the experimental and simulated results, the model still presented a good estimation of the system and can be used for preliminary studies.

## 5.2 Outlook

This thesis further developed the understanding of modeling, simulation and optimization of adsorption-based separation processes. The computational model developed in-house showed good results when used to model and simulate the adsorption unit from TDA Research Inc. Laboratory experiments or single-objective optimization could be used to finely tune the assumed coefficients in order to best fit the temperature profiles and the extract/raffinate purity and recovery. The pilot-scale PSA unit was relocated to an IGCC power plant facility in China, where more tests will be run with different operating conditions. The new data collected can be used to further enhance the model. To close the loop, the enhanced model can be used to test and optimize different cycles *in silico*, which can then be tested on the field.

For both $CO_2$ capture with reduced recovery and BP-SMB with reduced purity studies, it was shown that notable process improvements can be achieved under certain conditions. Even though energy consumption and process productivity are two good representatives of the overall process performance, no economical analysis has been included in this thesis. A complete economical

analysis would provide a better understanding of the trade-off between energy and productivity. It can also show the impact of the equipment and adsorbent prices, while economically quantifying the drawbacks of operating the PSA columns at very low pressures.

# Bibliography


[1] R. Haghpanah, A. Majumder, R. Nilam, A. Rajendran, S. Farooq, I. A. Karimi, and M. Amanullah, "Multi-objective optimization of a 4-step adsorption process for post-combustion $CO_2$ capture using finite volume technique," *Ind. Eng. Chem. Res.*, vol. 52, pp. 4249–4265, 2013.

[2] D. M. Ruthven, *Principles of adsorption and adsorption processes*. New York: John Wiley, 1984.

[3] A. Rajendran, "Recent developments in preparative chromatographic processes," *Curr. Opin. Chem. Engg.*, vol. 2, pp. 263–270, 2013.

[4] D. Y. C. Leung, G. Caramanna, and M. M. Maroto-Valer, "An overview of current status of carbon dioxide capture and storage technologies," *Renewable and Sustainable Energy Review*, no. 426-443, 2014.

[5] "The global status of CCS: 2017," tech. rep., Global Carbon Capture and Storage Institute, 2017.

[6] L. Riboldi and O. Bolland, "Overview on pressure swing adsorption (PSA) as $CO_2$ capture technology: state-of-the-art, limits and potential," *13th International Conference on Greenhouse Gas Control Technology*, no. 14-18, 2016.

[7] S. Choi, D. J. H., and C. W. Jones, "Adsorbent materials for carbon dioxide capture from large atmospheric point sources," *ChemSusChem*, vol. 2, no. 9, pp. 796–854, 2009.

[8] R. V. Siriwardane, M.-S. Shen, E. P. Fisher, and J. A. Poston, "Adsorption of $CO_2$ on molecular sieves and activated carbon," *Energy Fuels*, vol. 15, no. 2, pp. 279–284, 2001.

[9] M. Khurana and S. Farooq, "Adsorbent screening for post-combustion $CO_2$ capture: A method relating equilibrium isotherm characteristics to an optimum vacuum swing adsorption process performance," *Ind. Eng. Chem. Res.*, vol. 55, no. 8, pp. 2447–2460, 2016.

[10] R.-M. Nicoud, *Chromatographic Processes*. Cambridge University Press, 2015.

[11] D. M. Ruthven and C. B. Ching, "Counter-current and simulated counter-current adsorption separation processes," *Chem. Eng. Sci.*, vol. 44, no. 5, pp. 1011–1038, 1989.

[12] A. Rajendran, G. Paredes, and M. Mazzotti, "Simulated moving bed chromatography for the separation of enantiomers," *J. Chromatogr. A*, vol. 1216, no. 4, pp. 709–738, 2009.

[13] R.-M. Nicoud, "The amazing ability of continuous chromatography to adapt to a moving environment," *Ind. Eng. Chem. Res.*, vol. 53, no. 10, pp. 3755–3765, 2014.

[14] M. Amanullah and M. Mazzotti, "Optimization of a hybrid chromatography-crystallization process for the separation of Troger's base enantiomers," *J. Chromatogr. A*, vol. 1107, no. 1-2, pp. 36–45, 2006.

[15] J. Siitonen, T. Sainio, and A. Rajendran, "Bypass chromatography–design and analysis of an improved strategy for operating batch chromatography processes," *J. Chromatogr. A*, vol. 1230, pp. 77–92, 2012.

[16] J. Siitonen, T. Sainio, and A. Rajendran, "Design of batch chromatography for separation of binary mixtures under reduced purity requirements," *J. Chromatogr. A*, vol. 1286, pp. 55–68, 2013.

[17] M. Mazzotti, G. Storti, and M. Morbidelli, "Optimal operation of simulated moving bed units for nonlinear chromatographic separations," *J. Chromatogr. A*, vol. 769, no. 1, pp. 3–24, 1997.

[18] H. K. Rhee, R. Aris, and N. R. Amundson, *First-order partial differential equations*, vol. I. Mineola, N.Y.: Dover Publications, 2001.

[19] M. Mazzotti and A. Rajendran, "Equilibrium theory-based analysis of nonlinear waves in separation processes," *Annu. Rev. Chem. Biomol. Eng.*, vol. 4, pp. 119–141, 2013.

[20] A. Rajendran, "Equilibrium theory-based design of simulated moving bed processes under reduced purity requirements: Linear isotherms," *J. Chromatogr. A*, vol. 1185, no. 2, pp. 216–222, 2008.

[21] M. Mazzotti, "Equilibrium theory based design of simulated moving bed processes for a generalized langmuir isotherm," *J. Chromatogr. A*, vol. 1126, no. 1-2, pp. 311–322, 2006.

[22] M. Kaspereit, A. Seidel-Morgenstern, and A. Kienle, "Design of simulated moving bed processes under reduced purity requirements," *J. Chromatogr. A*, vol. 1162, pp. 2–13, 2007.

[23] M. Fütterer, "Design of simulated moving bed plants for reduced purities," *Chem. Engg. Technol.*, vol. 33, no. 1, pp. 21–34, 2010.

[24] S. Katsuo and M. Mazzotti, "Intermittent simulated moving bed chromatography: 1. Design criteria and cyclic steady-state," *J. Chromatogr. A*, vol. 1217, no. 8, pp. 1354–1361, 2010.

[25] S. Jermann, S. Katsuo, and M. Mazzotti, "Intermittent simulated moving bed processes for chromatographic three-fraction separation," *Org. Process Res. Dev.*, vol. 16, no. 2, pp. 311–322, 2012.

[26] D. C. Azevedo and A. E. Rodrigues, "Fructose–glucose separation in a SMB pilot unit: modeling, simulation, design, and operation," *AIChE journal*, vol. 47, no. 9, pp. 2042–2051, 2001.

[27] D. C. Azevedo and A. E. Rodrigues, "Design methodology and operation of a simulated moving bed reactor for the inversion of sucrose and glucose–fructose separation," *Chem. Eng. J.*, vol. 82, no. 1-3, pp. 95–107, 2001.

[28] IPCC, *Climate change 2014: Mitigation of Climate Change*, vol. 3. Cambridge University Press, 2015.

[29] N. Stern, "The economics of climate change," *Am. Econ. Rev.*, vol. 98, no. 2, pp. 1–37, 2008.

[30] J. Katzer, E. Moniz, J. Deutch, S. Ansolabehere, J. Beer, *et al.*, "The future of coal: an interdisciplinary MIT study," tech. rep., Technical report, Massachusetts Institute of Technology, Cambridge, MA, 2007.

[31] M. Bui, C. S. Adjiman, A. Bardow, E. J. Anthony, A. Boston, S. Brown, P. S. Fennell, S. Fuss, A. Galindo, and L. A. Hackett, "Carbon capture and storage (CCS): the way forward," *Energy Environ. Sci*, vol. 11, pp. 1062–1176, 2018.

[32] H. J. Herzog, *Carbon Capture*. MIT Press, 2018.

[33] A. Samanta, A. Zhao, G. K. Shimizu, P. Sarkar, and R. Gupta, "Post-combustion $CO_2$ capture using solid sorbents: a review," *Ind. Eng. Chem. Res.*, vol. 51, no. 4, pp. 1438–1463, 2011.

[34] M. Wang, A. Lawal, P. Stephenson, J. Sidders, and C. Ramshaw, "Post-combustion $CO_2$ capture with chemical absorption: A state-of-the-art review," *Chem. Eng. Res. Des.*, vol. 89, no. 9, pp. 1609–1624, 2011.

[35] D. Ko, R. Siriwardane, and L. T. Biegler, "Optimization of a pressure-swing adsorption process using zeolite 13X for $CO_2$ sequestration," *Ind. Eng. Chem. Res.*, vol. 42, no. 2, pp. 339–348, 2003.

[36] M. Khurana and S. Farooq, "Simulation and optimization of a 6-step dual-reflux VSA cycle for post-combustion $CO_2$ capture," *Chem. Eng. Sci*, vol. 152, pp. 507–515, 2016.

[37] K. S. Lackner, "A guide to $CO_2$ sequestration," *Science*, vol. 300, no. 5626, pp. 1677–1678, 2003.

[38] H. C. Mantripragada, H. Zhai, and E. S. Rubin, "Boundary Dam or Petra Nova–Which is a better model for CCS energy supply?," *Int. J. Greenh. Gas Control*, vol. 82, pp. 59–68, 2019.

[39] D. Y. Leung, G. Caramanna, and M. M. Maroto-Valer, "An overview of current status of carbon dioxide capture and storage technologies," *Renew. Sustain. Energy Rev.*, vol. 39, pp. 426–443, 2014.

[40] S. Krishnamurthy, V. R. Rao, S. Guntuka, P. Sharratt, R. Haghpanah, A. Rajendran, M. Amanullah, I. A. Karimi, and S. Farooq, "$CO_2$ capture from dry flue gas by vacuum swing adsorption: A pilot plant study," *AIChE J.*, vol. 60, no. 5, pp. 1830–1842, 2014.

[41] L. Wang, Y. Yang, W. Shen, X. Kong, P. Li, J. Yu, and A. E. Rodrigues, "$CO_2$ capture from flue gas in an existing coal-fired power plant by two successive pilot-scale VPSA units," *Ind. Eng. Chem. Res.*, vol. 52, no. 23, pp. 7947–7955, 2013.

[42] P. Xiao, J. Zhang, P. Webley, G. Li, R. Singh, and R. Todd, "Capture of $CO_2$ from flue gas streams with zeolite 13X by vacuum-pressure swing adsorption," *Adsorption*, vol. 14, no. 4-5, pp. 575–582, 2008.

[43] L. E. Perez, P. Sarkar, and A. Rajendran, "Experimental validation of multi-objective optimization techniques for design of vacuum swing adsorption processes," *Sep. Purif. Technol.*, vol. 224, pp. 553–563, 2019.

[44] V. Chou, A. K. S. Iyengar, V. Shah, and M. Woods, "Cost and performance baseline for fossil energy plants supplement: Sensitivity to $CO_2$ capture rate in coal-fired power plants," 2015.

[45] K. Deb, A. Pratap, S. Agarwal, and T. Meyarivan, "A fast and elitist multi-objective genetic algorithm: NSGA-II," *IEEE Trans. Evol. Comput.*, vol. 6, pp. 182–197, Apr 2002.

[46] S. Xiang, Y. He, Z. Zhang, H. Wu, W. Zhou, R. Krishna, and B. Chen, "Microporous metal-organic framework with potential for carbon dioxide capture at ambient conditions," *Nat. Commun.*, vol. 3, p. 954, 2012.

[47] B. J. Maring and P. A. Webley, "A new simplified pressure/vacuum swing adsorption model for rapid adsorbent screening for $CO_2$ capture applications," *Int. J. Greenh. Gas Control*, vol. 15, no. 0, pp. 16 – 31, 2013.

[48] M. Khurana and S. Farooq, "Integrated adsorbent–process optimization for carbon capture and concentration using vacuum swing adsorption cycles," *AIChE J.*, 2016.

[49] A. K. Rajagopalan, A. M. Avila, and A. Rajendran, "Do adsorbent screening metrics predict process performance? A process optimization based study for post-combustion capture of $CO_2$," *Int. J. Greenh. Gas Control*, vol. 46, pp. 76–85, 2016.

[50] R. Haghpanah, R. Nilam, A. Rajendran, S. Farooq, and I. A. Karimi, "Cycle synthesis and optimization of a VSA process for post-combustion $CO_2$ capture," *AIChE J.*, vol. 59, pp. 4735–4748, August 2013.

[51] A. Gokhan, A. Jayaraman, and M. Bonnema, "Highly efficient warm gas carbon capture for IGCC power plants," 2017. Presented at 2017 AIChE Annual Meeting, Session 57: Carbon Dioxide Capture from Power Generation.

[52] S. G. Subraveti, "Adsorption and chromatographic processes: Modeling and optimization," Master's thesis, University of Alberta.

[53] K. N. Pai, "A study on pressure vacuum swing adsorption based process design for carbon dioxide capture," Master's thesis, University of Alberta.

[54] N. S. Wilkins, "Characterizing adsorbents for pre- and post-combustion carbon capture," Master's thesis, University of Alberta.

[55] A. K. Rajagopalan, "Material selection and process design for adsorptive $CO_2$ capture," Master's thesis, University of Alberta.

# Appendix A

# Model equations for PSA simulations

Table A.1: Constitutive equations used to model the adsorption columns [1]

| Model equations |
|---|
| **Total mass balance** |
| $\frac{1}{P}\frac{\partial P}{\partial t} - \frac{1}{T}\frac{\partial T}{\partial t} = -\frac{T}{P}\frac{\partial}{\partial z}\left(\frac{P}{T}v\right) - \frac{RT}{P}\frac{1-\varepsilon}{\varepsilon}\sum_{\mathrm{i}=1}^{n_{\mathrm{comp}}}\frac{\partial q_{\mathrm{i}}}{\partial t}$ |
| **Component mass balance** |
| $\frac{\partial y_{\mathrm{i}}}{\partial t} + \frac{y_{\mathrm{i}}}{T}\frac{\partial P}{\partial t} - \frac{y_{\mathrm{i}}}{P}\frac{\partial T}{\partial t} = \frac{T}{P}D_L\frac{\partial}{\partial z}\left(\frac{P}{T}\frac{\partial y_{\mathrm{i}}}{\partial z}\right) - \frac{T}{P}\frac{\partial}{\partial z}\left(\frac{y_{\mathrm{i}}P}{T}v\right) - \frac{RT}{P}\frac{1-\varepsilon}{\varepsilon}\frac{\partial q_{\mathrm{i}}}{\partial t}$ |
| **Solid phase balance described by the LDF model** |
| $\frac{\partial q_{\mathrm{i}}}{\partial t} = k_{\mathrm{i}}(q_{\mathrm{i}}^{*} - q_{\mathrm{i}})$ |
| **Pressure drop calculated by Darcy's law** |
| $-\frac{\partial P}{\partial z} = \frac{4}{150}\frac{1}{r_{\mathrm{p}}^2}\left(\frac{1-\varepsilon}{\varepsilon}\right)^2\mu v$ |
| **Column energy balance** |
| $\left[\frac{1-\varepsilon}{\varepsilon}\left(\rho_{\mathrm{s}}C_{p,\mathrm{s}} + C_{p,\mathrm{a}}\sum_{\mathrm{i}=1}^{n_{\mathrm{comp}}}q_{\mathrm{i}}\right)\right]\frac{\partial T}{\partial t} = \frac{K_z}{\varepsilon}\frac{\partial^2 T}{\partial z^2} - \frac{C_{p,\mathrm{g}}}{R}\frac{\partial P}{\partial t} - \frac{C_{p,\mathrm{g}}}{R}\frac{\partial}{\partial z}(vP)$ |
| $-\frac{1-\varepsilon}{\varepsilon}C_{p,\mathrm{a}}T\sum_{\mathrm{i}=1}^{n_{\mathrm{comp}}}\frac{\partial q_{\mathrm{i}}}{\partial t} + \frac{1-\varepsilon}{\varepsilon}\sum_{\mathrm{i}=1}^{n_{\mathrm{comp}}}\left((-\Delta H)\frac{\partial q_{\mathrm{i}}}{\partial t}\right) - \frac{2h_{\mathrm{in}}}{\varepsilon r_{\mathrm{in}}}(T - T_{\mathrm{w}})$ |
| **Wall energy balance** |
| $\rho_{\mathrm{w}}C_{p,\mathrm{w}}\frac{\partial T_{\mathrm{w}}}{\partial t} = K_{\mathrm{w}}\frac{\partial^2 T_{\mathrm{w}}}{\partial z^2} + \frac{2r_{\mathrm{in}}h_{\mathrm{in}}}{r_{\mathrm{out}}^2 - r_{\mathrm{in}}^2}(T - T_{\mathrm{w}}) - \frac{2r_{\mathrm{out}}h_{\mathrm{out}}}{r_{\mathrm{out}}^2 - r_{\mathrm{in}}^2}(T_{\mathrm{w}} - T_{\mathrm{a}})$ |

Table A.2: Boundary conditions for PSA modeling [1]

| | $z = 0$ | $z = L$ |
|---|---|---|
| **OPEN-OPEN** | $v\|_{\mathrm{z=0}} = v_{\mathrm{feed}}$<br>$D_L \left.\frac{\partial y_{\mathrm{i}}}{\partial z}\right\|_{\mathrm{z=0}} = -v\|_{\mathrm{z=0}} \left(y_{\mathrm{i,feed}} - y_{\mathrm{i}}\|_{\mathrm{z=0}}\right)$<br>$K_z \left.\frac{\partial,T}{\partial z}\right\|_{\mathrm{z=0}} = -\varepsilon\, v\|_{\mathrm{z=0}}\, \rho_{\mathrm{g}} C_{p,\mathrm{g}} (T_{\mathrm{feed}} - T\|_{\mathrm{z=0}})$<br>$T_{\mathrm{w}}\|_{\mathrm{z=0}} = T_{\mathrm{a}}$ | $P\|_{\mathrm{z=L}} = P_2$<br>$\left.\frac{\partial y_{\mathrm{i}}}{\partial z}\right\|_{\mathrm{z=L}} = 0$<br>$\left.\frac{\partial T}{\partial z}\right\|_{\mathrm{z=L}} = 0$<br>$T_{\mathrm{w}}\|_{\mathrm{z=L}} = T_{\mathrm{a}}$ |
| **OPEN-CLOSED** | $P\|_{\mathrm{z=0}} = P_2 + (P_1 - P_2) e^{(-\alpha_p t)}$<br>$D_L \left.\frac{\partial y_{\mathrm{i}}}{\partial z}\right\|_{\mathrm{z=0}} = -v\|_{\mathrm{z=0}} \left(y_{\mathrm{i,feed}} - y_{\mathrm{i}}\|_{\mathrm{z=0}}\right)$<br>$K_z \frac{\partial \mathrm{T}}{\partial \mathrm{z}}\|_{\mathrm{z=0}} = -\varepsilon\, v\|_{\mathrm{z=0}}\, \rho_{\mathrm{g}} C_{p,\mathrm{g}} (T_{\mathrm{feed}} - T\|_{\mathrm{z=0}})$<br>$T_{\mathrm{w}}\|_{\mathrm{z=0}} = T_{\mathrm{a}}$ | $\left.\frac{\partial P}{\partial \mathrm{z}}\right\|_{\mathrm{z=L}} = 0$<br>$\left.\frac{\partial y_{\mathrm{i}}}{\partial \mathrm{z}}\right\|_{\mathrm{z=L}} = 0$<br>$\left.\frac{\partial \mathrm{T}}{\partial \mathrm{z}}\right\|_{\mathrm{z=L}} = 0$<br>$T_{\mathrm{w}}\|_{\mathrm{z=L}} = T_{\mathrm{a}}$ |
| **CLOSED-OPEN** | $v\|_{\mathrm{z=0}} = 0$<br>$\left.\frac{\partial y_{\mathrm{i}}}{\partial z}\right\|_{\mathrm{z=0}} = 0$<br>$\left.\frac{\partial T}{\partial z}\right\|_{\mathrm{z=0}} = 0$<br>$\left.\frac{\partial P}{\partial z}\right\|_{\mathrm{z=0}} = 0$ | $P\|_{\mathrm{z=L}} = P_1 + (P_2 - P_1) e^{(-\alpha_p t)}$<br>$\left.\frac{\partial y_{\mathrm{i}}}{\partial z}\right\|_{\mathrm{z=L}} = 0$<br>$\left.\frac{\partial T}{\partial z}\right\|_{\mathrm{z=L}} = 0$<br>$T_{\mathrm{w}}\|_{\mathrm{z=L}} = T_{\mathrm{a}}$ |

# Appendix B

# Supporting information for Chapter 3

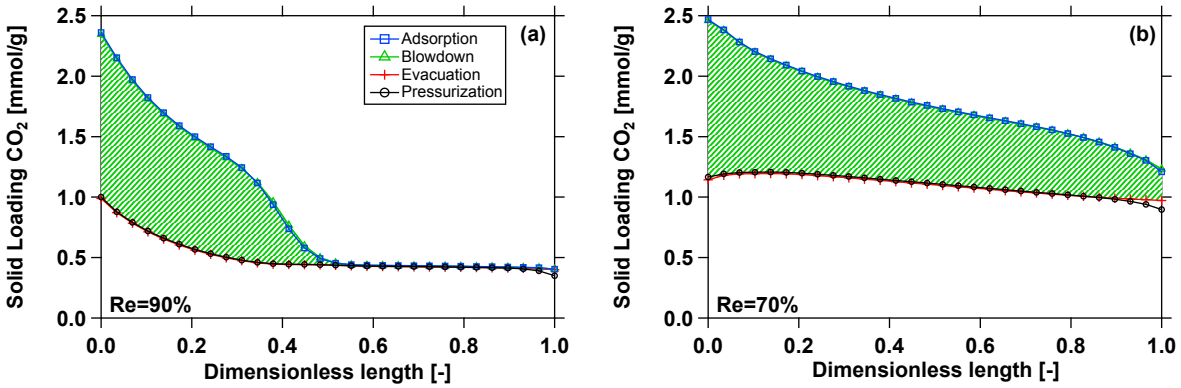


Figure B.1: Solid loading of $CO_2$ in UTSA-16 in each stage of the 4-step PSA cycle with 95% purity and varying recoveries: (a) Re =90% and (b) Re =70%. The shaded region in each plot represents the amount of $CO_2$ extracted during the evacuation step.

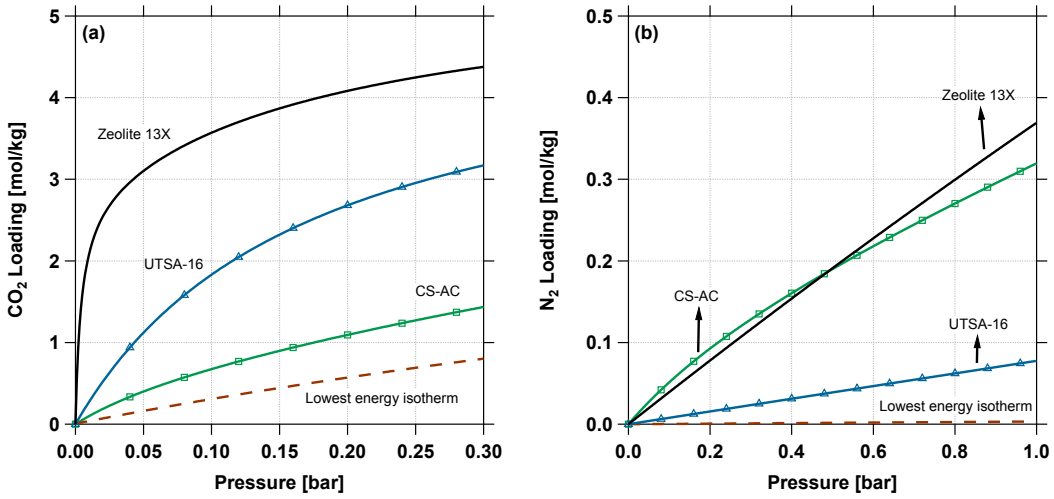


Figure B.2: Adsorption equilibrium curves of (a) $CO_2$ and (b) $N_2$ at 25°C for different materials.